



ÉCOLE
POLYTECHNIQUE
DE BRUXELLES



UNIVERSITÉ LIBRE DE BRUXELLES

Interferometric stabilisation of a fibre-based optical computer

Experimental study

Mémoire présenté en vue de l'obtention du diplôme
d'Ingénieur Civil physicien à finalité spécialisée

Denis Verstraeten

Directeur

Professeur Marc Haelterman

Co-Promoteur

Professeur Serge Massar

Superviseur

Lorenz Butschek

Service

Opera

Année académique
2018 - 2019

Abstract

Acknowledgements

Contents

| | | |
|----------|---|-----------|
| 1 | Introduction | 6 |
| 2 | Reservoir Computing | 7 |
| 2.1 | Reservoir Computing framework | 7 |
| 2.1.1 | Artificial Neural Network | 7 |
| 2.1.2 | Reservoir Computing | 8 |
| 2.1.3 | Machine Learning | 8 |
| 2.2 | Mathematical Model | 9 |
| 2.2.1 | Dynamics of the reservoir | 10 |
| 2.2.2 | Computation of the output weights | 11 |
| 2.3 | Introduction to Photonic Reservoir Computing | 11 |
| 2.3.1 | Time Division Multiplexing of the neurons | 12 |
| 2.3.2 | Simplifying assumptions | 12 |
| 2.3.3 | Neurons encoded in light intensity | 13 |
| 2.3.4 | Neurons encoded in phaser representation of the electric field | 14 |
| 2.3.5 | Simulations | 15 |
| 3 | Photonic Reservoir Computer with Wavelength Division Multiplexed neurons | 17 |
| 3.1 | Description of the scheme | 17 |
| 3.1.1 | Working principle | 18 |
| 3.1.2 | Frequency coupling of the neurons | 19 |
| 3.1.3 | Mathematical model | 20 |
| 4 | Interferometric stabilisation of reservoir cavity | 22 |
| 4.1 | Introduction | 22 |
| 4.1.1 | Fabry-Perot interferometer | 22 |
| 4.1.2 | Ring cavity | 24 |
| 4.1.3 | Challenge | 24 |
| 4.2 | Experimental setup | 26 |
| 4.3 | Characterisation of the reservoir | 28 |
| 4.3.1 | Transfer function of the cavity | 28 |
| 4.3.2 | Effective losses | 33 |
| 4.3.3 | Modulation depth | 34 |
| 4.4 | Pound-Drever-Hall stabilisation technique | 35 |
| 4.4.1 | Introduction | 35 |
| 4.4.2 | Pound-Drever-Hall scheme | 37 |
| 4.4.3 | Pound-Drever-Hall technique for the reservoir | 39 |
| 4.5 | Characterisation of the stabilisation performance for different regimes | 40 |
| 4.5.1 | Introduction | 40 |
| 4.5.2 | Approach | 41 |

| | |
|-------------------------------|-----------|
| 4.5.3 Results | 48 |
| 5 Conclusion | 50 |
| A Experimental results | 51 |
| B Specifications | 59 |
| Acronyms | 60 |

Chapter 1

Introduction

Chapter 2

Reservoir Computing

Reservoir Computing (RC) is a bio-inspired artificial Recurrent Neural Network (RNN) which is based on the Echo State Network (ESN) introduced by Herbert Jaeger in [17]. This computation scheme is well suited for real-time data processing and for chaotic time series prediction[17, 18, 24], and achieves state of the art performances in those domains, as well as in speech recognition[43, 40, 21], nonlinear channel equalisation[17] and financial forecasting [3].

The first section of this chapter introduces the different concepts linked with RC. It starts by giving a brief overview on the Neural Network (NN) computation paradigm from which RC has been derived. After that, the structure, operating principles and features of Reservoir Computer (RC) are presented. Then, a few elements of Machine Learning (ML) are mentioned in order to have a first glimpse of the training procedure for RC. The second section is devoted to the mathematical model governing a RC. The last section is about Photonic Reservoir Computers. During the last decade, several physical implementations of RC have been proposed, some of which being optical setups. This kind of RC is presented, and most specifically reservoir involving Time Division Multiplexing (TDM). Finally, a RC is used to resolve two different benchmark tasks and the results on the computations are shown.

2.1 Reservoir Computing framework

2.1.1 Artificial Neural Network

A RC is specific kind of NN, which is a computation paradigm mimicking the behaviour of a biological brain. The artificial neurons are simply interconnected entities carrying an activation level. The way the activation level is updated depends on the scheme, but the basic idea is common for all of them: a neuron receives a linear combination of the activation level of the neurons to which it is connected, and then computes a nonlinear transformation of this value. This gives the new activation level. On figure 2.1, a feedforward NN is depicted. It is called feedforward because the computation goes from left (input neurons in red) to right (output neurons in green). Feedforward NN are organised in layers, and a neuron from one layer can only be influenced by neurons in the adjacent layers. This is shown on the Figure by the arrows representing the connections. The gray neurons in the middle belong to the hidden layers, which are used to improve the computing power of such networks. The results of a computation can be read on the activation level of the output neurons [36, p.727][4, p.225].

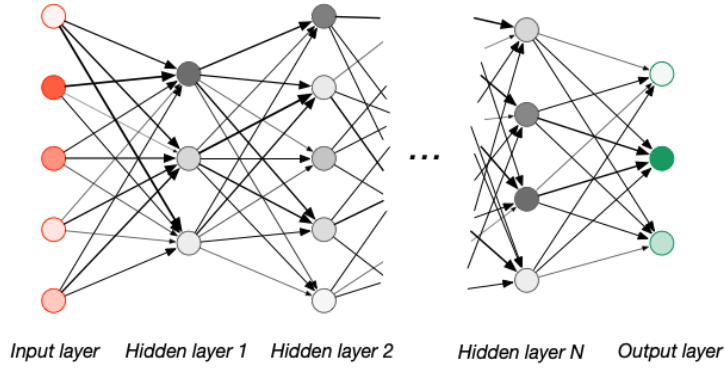


Figure 2.1: Schematic representation of a feedforward NN

2.1.2 Reservoir Computing

RC have been designed to process time dependent inputs, so their structure is inherently different from that of a feedforward NN, because they need to exhibit other properties. In this scheme, all the neurons are interconnected and form what is called a reservoir. The reservoir is fed with the time dependent input signal it should process. When the reservoir is properly set up, the activation level of each of the neurons becomes a systematic transformed version of the input signal [17]. This operating point is called the echo state and allows RC to reach their best performances [16, 18]. In this regime, RC exhibit a short-term memory of the previous inputs [17], which could explain why they perform so well in time dependent situations. There are many physical implementations of RC proposed in the literature, many of which are based on optical setups [37], that is why section 2.3 is devoted to them.

On figure 2.2, a RC is shown. The neurons of the reservoir are represented in orange. They characterise what is called the state of the reservoir, which is encoded by $\mathbf{x}(t)$. They are coupled by the connection matrix \mathbf{W} . The input signal $u(t)$ is fed into the input neuron (blue) and is coupled to the reservoir *via* the input matrix \mathbf{W}^{in} . The output $y(t)$ is read on the output neuron (red) and is obtained thanks to the output matrix \mathbf{W}^{out} . This matrix is the only one that needs to be updated when the reservoir is learning. This task is not straightforward, that is why the next paragraph takes care of introducing the different approaches that can be followed to compute \mathbf{W}^{out} . For some applications, it can be useful to also have a feedback of the output sent back into the reservoir. This can be achieved by the feedback matrix \mathbf{W}^{fb} . The mathematical aspects mentioned in this paragraph are detailed in section 2.2.

2.1.3 Machine Learning

Regardless of the learning scheme used to train a NN, the basic idea is always to minimise the difference between the desired and the actual outputs. In practice, this is achieved by updating the different connection coefficients of the NN [4, p.233][36, p.733]. This procedure often turns out to be a really complicated task for feedforward NN, which explains why the development of efficient ML algorithms is such a hot topic nowadays. In contrast, as can be seen on figure 2.3, RC only need their output weights to be adjusted when being trained, which makes them computationally lighter [17]. This is due to the fact that the connections of the reservoir should not contain any information about the task, but should only be used to reach the ESN regime, as mentioned in the previous paragraph. There are two main families of training methods for RC [19]. On the one

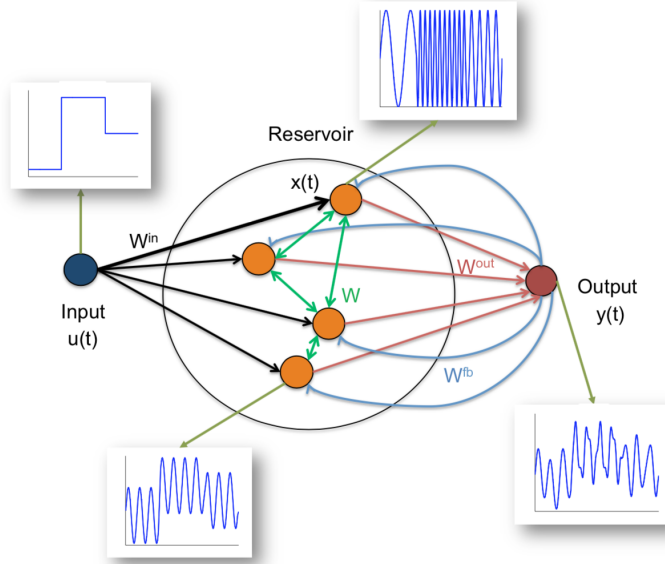


Figure 2.2: Schematic representation of a Reservoir Computer [3]

hand, there is the *batch learning*, which comprises the methods requiring to first store a wealth of data regarding the task being taught before being able to actually compute the output weights. Once enough data is gathered, this kind of algorithms returns the optimal weights all at once. They present the advantage of involving only one training phase, after which the RC are ready to perform. However, the need for vast amount of data and the inability for the RC to adapt to an input evolving out of the range for which it has been trained are two drawbacks. On the other hand, *online learning* methods allow to iteratively improve the output weights. Therefore, starting from a first guess, these algorithms can converge to suitable output weights. They are much more adaptable than the batch learning ones. However, their convergence is not guaranteed and can be slow [20, 38].

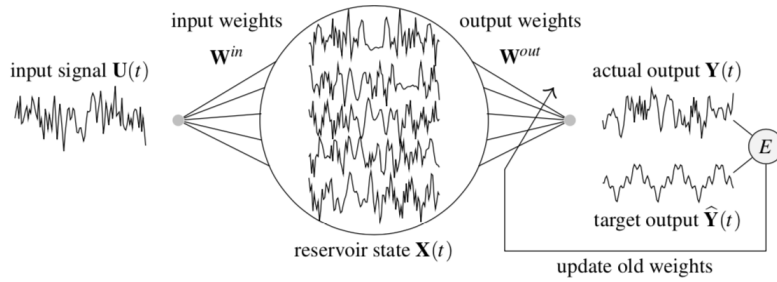


Figure 2.3: Learning procedure for Reservoir Computer [16]

2.2 Mathematical Model

In this section, an overview of the mathematical framework is given. First, the different objects are formally defined, and their dynamics is presented. Then, a few key elements about the computation of the output weights are introduced.

2.2.1 Dynamics of the reservoir

let us define the *state* of the reservoir. As said previously, the RC can be fully described by the activation level of each of its neurons. The state is therefore defined as a vector whose components are the activation levels of the neurons. If the number of neurons making up the reservoir is N , and if x_i is the activation level of the i^{th} neuron, then the state vector reads as follows:

$$\mathbf{x} = \begin{bmatrix} x_1 \\ \vdots \\ x_i \\ \vdots \\ x_N \end{bmatrix} \quad (2.1)$$

The dynamics governing the state vector and the output of the reservoir proposed in [18] are presented below. In practice, it is too general for the implementations studied in this work. However, the equations are introduced without loss of generality, and simplifying assumptions applying the photonic implementations of RC will be specified in the section devoted to them.

$$\mathbf{x}(n+1) = \mathbf{f}(\mathbf{W}^{\text{in}}\mathbf{u}(n+1) + \mathbf{W}\mathbf{x}(n) + \mathbf{W}^{\text{fb}}\mathbf{y}(n)) \quad (2.2)$$

$$\mathbf{y}(n+1) = \mathbf{f}^{\text{out}}(\mathbf{W}^{\text{out}}(\mathbf{x}(n+1), \mathbf{u}(n+1), \mathbf{y}(n))) \quad (2.3)$$

Different elements need to be defined:

- $n \in \{1, \dots, T\}$ is the discrete time variable
- $\mathbf{u} \in \mathbb{C}^k$ is the input vector which enters the reservoir through the input neurons
- $\mathbf{W}^{\text{in}} \in \mathbb{C}^{N \times k}$ is the input matrix. It indicates how the k input neurons are connected to the neurons of the reservoir
- $\mathbf{x} \in \mathbb{C}^N$ is the state vector, as said previously
- $\mathbf{W} \in \mathbb{C}^{N \times N}$ is the synaptic matrix, or the connection matrix which has already been introduced
- $\mathbf{y} \in \mathbb{C}^m$ is the output vector of the reservoir whose value can be read out on the output neurons
- $\mathbf{W}^{\text{fb}} \in \mathbb{C}^{N \times m}$ is the feedback matrix. It couples the output back into the reservoir
- $\mathbf{f} : \mathbb{C}^N \mapsto \mathbb{C}^N$ is the nonlinear function mapping the linear combination it receives as argument to a valid state vector
- $(\mathbf{x}(n+1), \mathbf{u}(n+1), \mathbf{y}(n))$ is the concatenation of those three vectors
- $\mathbf{W}^{\text{out}} \in \mathbb{C}^{m \times (N+k+m)}$ is the output matrix of the reservoir. It is optimised through ML
- $\mathbf{f}^{\text{out}} : \mathbb{C}^m \mapsto \mathbb{C}^m$ is the output function of the reservoir

2.2.2 Computation of the output weights

To determine the output matrix \mathbf{W}^{out} in the batch learning approach, one needs to perform a ridge (or Tikhonov) regression [40], which is an improved version of multivariate linear regression that improves the numerical stability of the scheme, and that prevents overfitting of the data. By restricting the desired output to a scalar function $\hat{y}(n)$ and by taking a learning period of T time steps, one defines the matrices \mathbf{X} and $\hat{\mathbf{Y}}$ and solves the following equation to find the output weights vector \mathbf{W}^{out} :

$$\mathbf{X} = \begin{bmatrix} x_0(0) & x_1(0) & \dots & x_N(0) \\ x_0(1) & x_1(1) & \dots & x_N(1) \\ \vdots & & & \vdots \\ x_0(T) & x_1(T) & \dots & x_N(T) \end{bmatrix}, \quad \hat{\mathbf{Y}} = \begin{bmatrix} \hat{y}(0) \\ \hat{y}(1) \\ \vdots \\ \hat{y}(T) \end{bmatrix} \quad (2.4)$$

$$(\mathbf{X}^T \mathbf{X} + \varepsilon \mathbf{I}) \mathbf{W}^{\text{out}} = \mathbf{X}^T \hat{\mathbf{Y}} \quad (2.5)$$

Here ε is the constant used for the Tikhonov regression. By setting ε to 0, one finds the *normal equation* that comes up when solving a linear regression [16] in the sense of the least squares. This procedure can be generalised to higher dimensions desired output vectors $\hat{\mathbf{y}}(n)$. Different optimisation algorithms can be used to compute the output weights in practice, but their description is out of the scope of this work, see [23] for more details.

Different metrics can be used to capture the distance between the actual and the desired outputs. In the literature, one of the most frequent ones is the Normalised Mean Square Error (NMSE) [13] (with $\hat{\mathbf{y}}(n)$ the target vector, $\langle \dots \rangle_n$ the average with respect to n , and $\| \dots \|$ the euclidean norm):

$$\text{NMSE} = \frac{\langle \|\hat{\mathbf{y}}(n) - \mathbf{y}(n)\|^2 \rangle_n}{\langle \|\hat{\mathbf{y}}(n) - \langle \hat{\mathbf{y}}(n) \rangle_n \|^2 \rangle_n} \quad (2.6)$$

2.3 Introduction to Photonic Reservoir Computing

As already mentioned, different implementations of Photonic Reservoir Computing (PRC) have been proposed [37]. In this section, systems in which neurons are multiplexed in time are studied because they constitute a good first approach to PRC and because they bring insights that are interesting for the scheme explored in this thesis. However, it is worth mentioning that one can find among others spatially distributed RC based on fully integrated silicon-chip with nonlinearities stemming from Semiconductor Optical Amplifiers [41], and on diffractively coupled Vertical-Cavity Surface-Emitting Lasers [7].

In this section, the assumptions applying to reservoir with TDM of the neurons are first presented. Indeed, the equations introduced in the previous section can be substantially simplified when one is working with this kind of reservoir. After that, setups where neurons are encoded in the intensity of the light are considered. Finally, experiments in which the neurons are represented in the phaser of the electric field are presented. Recalling that the light intensity is proportional to the squared modulus of the phaser of the electric field, it is shown that the outputs of these two kinds of reservoir are different, but analogous, and that they rely on the same mathematical interpretation. The latter

scheme is studied with greater length since it reaches state of the art performances in classical benchmark tasks and since the novel implementation which is the main topic of this work shares some features with it. As a last remark, and to give a better understanding on the flexibility of RC, in [14] the researchers managed to perform speech recognition and to resolve the XOR problem¹ in a bucket of water.

2.3.1 Time Division Multiplexing of the neurons

Many implementations of RC based on TDM of the neurons have been proposed in the literature [30, 2, 13, 10, 42, 44]. Let T be the time scale of the input signal. It should be close to the Round Trip Time (RTT) of the delay line, but not exactly the same in order to be able to couple the neurons. The detuning between the RTT and T is controlled by the integer parameter k . On figure 2.4, one can observe how the neurons can be multiplexed in time. One can see that the allocated window for each of the neurons lasts $\theta = T/N$. Since θ cannot be arbitrarily small in practice², this implies that the greater the number of neurons, the greater T and thus the slower the time scale of the input data. This suggests that one should look for a tradeoff between accuracy and speed in data processing for this kind of RC. For example, in [44], the refresh rate of the input is around 0.9 GHz.

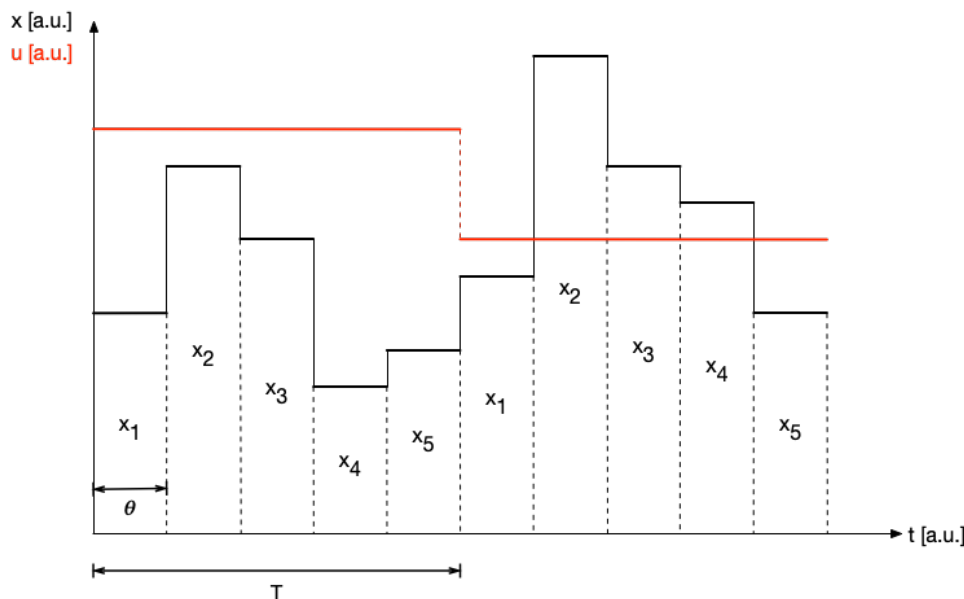


Figure 2.4: Schematic representation of the evolution of the neurons in time for a TDM reservoir

2.3.2 Simplifying assumptions

In this section, the mathematical framework introduced in section 2.2 is adapted to describe the behaviour of TDM PRC in a suitable way. Further details concerning specific types of PRC are added in the following sections which are devoted to them.

¹The XOR task consists in reproducing the behaviour of a logical XOR gate, which is a task of historical importance for NN [26].

²If θ gets too short, it exceeds the bandwidth of measurement devices, so it becomes impossible to measure the neurons.

Input and connection matrices The input of the reservoir is real scalar function $u(n)$ for PRC, therefore the expression of \mathbf{W}^{in} becomes a real vector of length N which is called the *input mask* \mathbf{m} in the literature. The input mask can be chosen in different ways: in [13], they use a sinusoidal input mask whereas in [2, 44, 30] the input masks are randomly chosen.

Very few constraints apply to the creation of the connection matrix \mathbf{W} . It can be randomly generated and sparse. However, to make the occurrence of the echo state more likely to happen, one wants to work with a spectral radius $\rho(\mathbf{W}) < 1$. If this condition is not verified, as well as degrading the performance of the reservoir, this can also lead to instabilities [23].

The matrices \mathbf{W} and \mathbf{W}^{in} can be rescaled, and this scaling can alter the performances of the reservoir. One should therefore design the PRC in such a way that those scaling factors are easily accessible experimentally. If one defines α and β , the feedback³ and input gains, the input and connection matrices become:

$$\mathbf{W} \longrightarrow \alpha \mathbf{A}, \quad \mathbf{W}^{\text{in}} \longrightarrow \beta \mathbf{m} \quad (2.7)$$

Feedback and output The output signal of a PRC is a real scalar function $y(n)$, which means that the output matrix \mathbf{W}^{out} becomes a real vector. Furthermore, the concatenation of $\mathbf{x}(n+1), \mathbf{u}(n+1), y(n)$ appearing in equation (2.3) is not used, but only the state vector \mathbf{x} , hence the fact that \mathbf{W}^{out} is of dimension N . Regarding the feedback of the output into the reservoir, it is currently not doable in practice. This is due to the fact that, when running a RC experiment, some post-processing of the data needs to be performed on a computer in order to obtain the output.

With all these simplifications, equations (2.2) and (2.3) reduce to:

$$\mathbf{x}(n+1) = \mathbf{f}(\alpha \mathbf{A} \mathbf{x}(n) + \beta \mathbf{m} u(n+1)) \quad (2.8)$$

$$y(n+1) = f^{\text{out}}(\mathbf{W}^{\text{out}} \mathbf{x}(n+1)) \quad (2.9)$$

2.3.3 Neurons encoded in light intensity

There are two major families of TDM PRC. The first kind of PRC are those using optical components exhibiting nonlinear behaviour, such as Mach-Zehnder Modulator (MZM) [13, 30, 2], Semiconductor Optical Amplifier (SOA) [42] or semiconductor saturable absorber mirror [10] to couple the neurons. In an actual optical experiment, the measurements have to be done with photodiodes. These devices can only inform about the intensity of the light, which is the squared modulus of the phaser representation of the electric field, and not about the actual electric field. However, in the scheme presented above, the input and the activation level of the neurons are real valued functions appropriately encoded in the intensity of the light, and can therefore be directly read out by a photodiode, hence this simple expression for the output of the reservoir:

$$y(n+1) = \sum_{i=1}^N W_i^{\text{out}} x_i(n+1) = (\mathbf{W}^{\text{out}})^{\text{T}} \cdot \mathbf{x}(n+1) \quad (2.10)$$

³This may seem like a misnomer at this point since it has nothing to do with \mathbf{W}^{fb} , but this name is used because α acts as a gain for the activation level of the neurons being fed back into the reservoir.

2.3.4 Neurons encoded in phaser representation of the electric field

On the other hand, in [44], coherent light is used and the neurons are encoded in the complex phaser representation of the electric field and are linearly coupled using a delay line. In this scheme, the reservoir is linear, as can be seen on equation (2.12). This kind of RC is described with greater length because the new approach studied in this thesis relies on a linear reservoir as well. In this equation, α and β are the feedback and input gains, respectively, A_0 is the input bias, ϕ is the phase acquired by the electric field during by going through the delay line, and k is the detuning parameter.

$$x_i(n+1) = \begin{cases} \alpha e^{j\phi} x_{i-k}(n) + \beta (m_i u(n) + A_0) & \text{if } k \leq i \leq N \\ \alpha e^{j\phi} x_{N+i-k}(n-1) + \beta (m_i u(n) + A_0) & \text{if } 0 \leq i \leq k \end{cases} \quad (2.11)$$

The equation can be rewritten in a compact way:

$$\mathbf{x}(n+1) = \alpha \mathbf{A} \mathbf{x}(n) + \beta (\mathbf{m} u(n+1) + \mathbf{A}_0) \quad (2.12)$$

It thus appears more clearly why the condition mentioned previously regarding $\rho(\alpha \mathbf{A})$ is relevant. Indeed, by neglecting the inputs, if \mathbf{x}_j is an eigenvector of $\alpha \mathbf{A}$ with eigenvalue $\lambda_j > 1$, the above equation will lead to an exponential divergence $\mathbf{x}_j(n) \sim \lambda_j^n \mathbf{x}_j(0)$. On the other hand, if λ_j is too small, the state \mathbf{x}_j will be damped too quickly, deteriorating the short-term memory capabilities of the reservoir and preventing it from reaching the echo state.

In the linear reservoir, since the neurons and the input are inscribed in the complex electric field, the nonlinearity is introduced by the read out photodiodes. The output is therefore given by:

$$y(n+1) = \sum_{i=1}^N W_i^{\text{out}} |x_i(n+1)|^2 \quad (2.13)$$

From a historical point of view, it is interesting to notice that this reservoir shares features with the first artificial NN, the *perceptron*, introduced by F. Rosenblatt in 1958 [35], which also had a linear connection matrix, and a nonlinear output function.

Equations (2.10) and (2.13) give an interesting intuition on the meaning of the ESN. Indeed, as said previously, when a RC reaches the echo state, each of the neurons tends to systematically reproduce a modified version of the input, the actual modification being an individual characteristic of each neuron [17]. One can see this feature in the perspective of linear algebra. When the RC is fed with an input, it creates a set of time varying functions that can be seen as a basis in which one can try to express the output of the reservoir, which is a vector in the vectorial space of functions. This is why it is often said in the literature that a RC maps an input to a higher dimensional space. Therefore, one can in theory approach any target function with an arbitrary precision, depending on the number of neurons in the reservoir [17]. The higher the number of neurons, the closer to a genuine series development one gets.

2.3.5 Simulations

In this section, the performance of the linear reservoir with quadratic output from [44] are estimated with simulations. Two benchmark task are tackled, first NARMA10 and then nonlinear channel equalisation.

NARMA10

Nonlinear Auto-Regressive Moving Average (NARMA) 10 is a model often used to simulate chaotic time series because it exhibits similar properties [30]. If $u(n)$ is a random variable uniformly distributed along the interval $[-0.5, 0.5]$, the recurrent equation for NARMA10 reads:

$$\hat{y}(n+1) = 0.3\hat{y}(n) + 0.05\hat{y}(n) \left(\sum_{i=0}^9 \hat{y}(n-i) \right) + 1.5u(n-9)u(n) + 0.1 \quad (2.14)$$

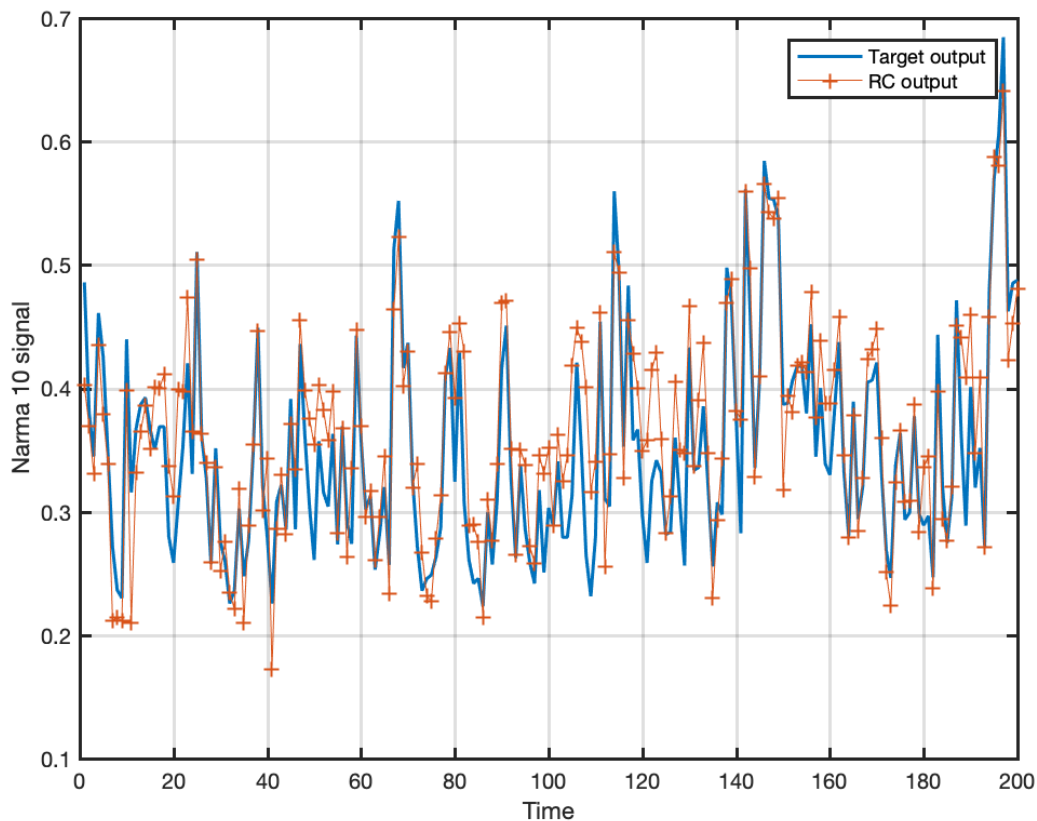


Figure 2.5: NARMA10 task with NMSE equal to 0.1541. This reservoir is made of 50 neurons. $\alpha = 0.5$, $k = 7$, $\phi = 0$ rad, $\beta = 1$, $A_0 = 1$, \mathbf{m} is a random vector distributed between 0 and 1. The first 300 time steps were discarded in order to let enough time to the reservoir to enter the echo state (washout). Then the reservoir was trained for 3000 time steps and tested over 6000 time steps. This reservoir is particularly well suited for NARMA10 since the nonlinearities in the signal are mostly quadratic.

Nonlinear channel equalisation

This task consists in the reconstruction of a signal after it has travelled through a non-linear channel. The emitted signal \hat{y} is randomly drawn from the symbol set $\{-3, -1, 1, 3\}$. It is first superposed with following and preceding symbols as can be seen in (2.15). After that, a third degree polynomial transformation is applied to the mixed signals, and a Gaussian noise, whose intensity can be set in order to adjust the signal to noise ratio, is added in (2.16). This metric used to evaluate the performance of the reservoir for this type of task is the Signal Error Rate (SER) and is defined as the ratio between the number of erroneous symbols and the total number of symbols.

$$\begin{aligned} q(n) = & 0.08\hat{y}(n+2) - 0.12\hat{y}(n+1) + \hat{y}(n) + 0.18\hat{y}(n-1) \\ & - 0.1\hat{y}(n-2) + 0.091\hat{y}(n-3) - 0.05\hat{y}(n-4) \\ & + 0.04\hat{y}(n-5) + 0.03\hat{y}(n-6) + 0.01\hat{y}(n-7) \end{aligned} \quad (2.15)$$

$$u(n) = q(n) + 0.036q(n)^2 - 0.011q(n)^3 + \nu(n) \quad (2.16)$$

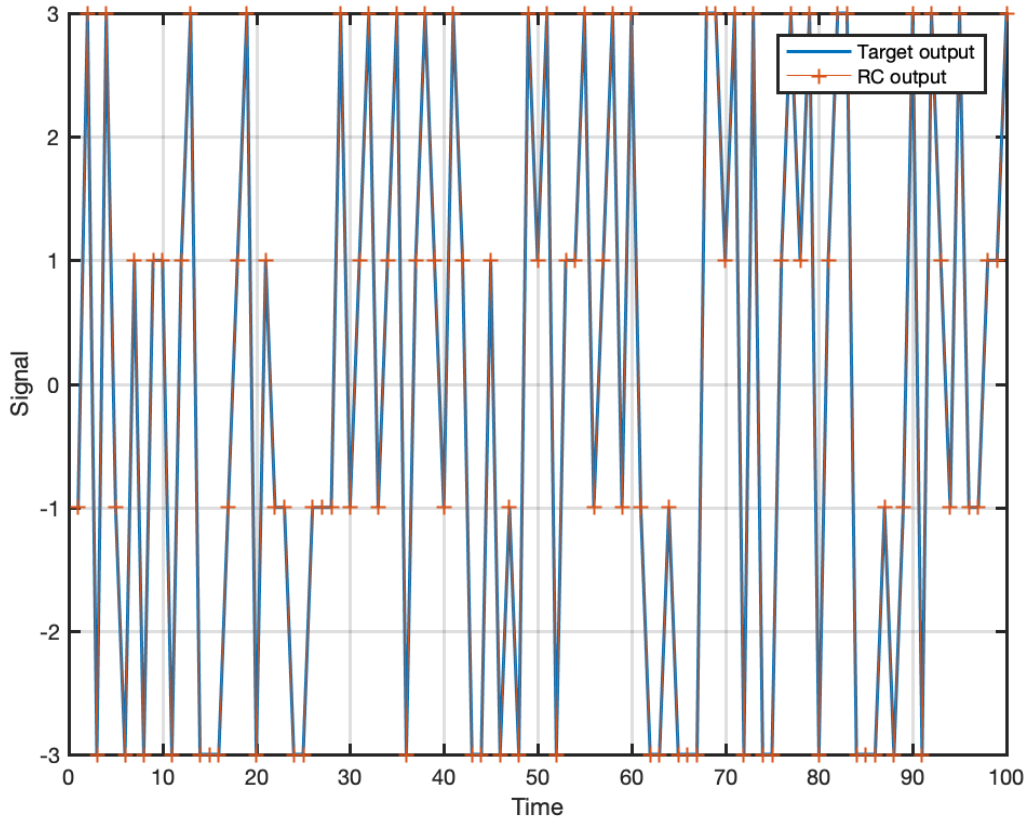


Figure 2.6: Nonlinear channel equalisation task with a signal error rate of $5 \cdot 10^{-4}$, with Signal to Noise Ratio (SNR) equal to 32 dB. This reservoir is made of 50 neurons. $\alpha = 0.5$, $k = 7$, $\phi = 0$ rad, $\beta = 1$, $A_0 = 1$, \mathbf{m} is a random vector distributed between 0 and 1. The first 300 time steps were discarded in order to let enough time to the reservoir to enter the echo state (washout). Then the reservoir was trained for 3000 time steps and tested over 6000 time steps. The symbols predicted by the RC are found by changing the continuous valued output by the closest symbol.

Chapter 3

Photonic Reservoir Computer with Wavelength Division Multiplexed neurons

In this chapter, a novel approach of PRC is proposed, in which the neurons are no longer multiplexed in time, but in wavelength (or frequency) instead. This scheme was introduced in [1] and its end goal is to overcome the speed limitations imposed by the TDM of the neurons, as exposed in section 2.4. Indeed, by multiplexing the neurons in the frequency domain, the input signal can reach them all in the same time, there is no need to slow down its pace to let it alter the neurons sequentially. As an illustration, in [41], they proposed the first PRC with parallelisation of the neurons. In the experiment described in the paper, the neurons were spatially multiplexed. Doing so, the authors were able to reach data processing rates up to 12.5 GHz on tasks such as header recognition or boolean logic, which is an increase of one order of magnitude compared to those reported in [44]. This is encouraging for research in parallel PRC and motivates the study of the scheme explored in this thesis.

First, in section 3.1, a description of the working principle is given. It starts with a high-level overview of the scheme in which different features and components are presented. After that, attention is brought to the frequency coupling mechanism used to let the neurons interact between one another. It is shown that this can be achieved using a optoelectronic Phase Modulator (PM), even though this device has some practical drawbacks. Finally, the scheme is described with more details. In section ??, the stabilisation issue, which is main topic of this thesis, is introduced.

3.1 Description of the scheme

In this section, the working principle of Wavelength Division Multiplexing (WDM) PRC is first given. This scheme takes advantage of the wave character of light and uses different wavelength to encode the neurons. It is fibre-based and relies on an optical cavity made of a fibre loop. Inside the resonator, the different neurons need to be able to interact, therefore one has to provide some coupling mechanism for the different frequencies. This issue is tackled in section 3.1.2 and provides interesting mathematical insights that are eventually used to derive a suitable model for this other kind of linear RC.

3.1.1 Working principle

The working principle of the new reservoir is schematised on figure 3.1. The whole setup is fibre-based, and the fibre used is a polarisation maintaining, single mode fibre.

Input The input time series $u(n)$ is converted into a continuous signal $\tilde{u}(t)$ by keeping its value constant during one period τ (sample and hold procedure), which leads to $\tilde{u}(t) = u(n)$, with $t \in [n\tau, (n+1)\tau[$. The continuous, coherent light emitted by a narrow band laser at frequency ω_0 is modulated in intensity by the input signal $\tilde{u}(t)$ using a MZM.

Cavity The modulated data is then coupled to a ring cavity around 20 metres long¹. Inside this cavity, a PM mixes the different optical frequencies. More information about the PM can be found in section 3.1.2. Losses are introduced inside the cavity by two main sources, the intrinsic losses of the fibre and the insertion losses of the PM, hence the presence of an intra-cavity amplifier used to compensate for them. The neurons are encoded in the electric field evolving inside this cavity, which is schematised on the figure by the three different colours for the fibre loops. Therefore, from now on, the cavity is referred to as the *reservoir*. The holding time τ introduced earlier should be equal to the RTT of the reservoir. This is done in order to update the discrete dynamics of the RC each time the light completes a trip around the cavity. Doing so, one ensures that the value of the neuron x_j at discrete time $n+1$ depends on the values of the neurons x_i , with $i \in \{1, \dots, N\}$, at precisely time n .

Readout The electric field encoding the neurons exits the cavity through another coupler, and is then demultiplexed in frequency. Each of the frequency component is measured using a Photodiode (PD), which gives a value proportional to the squared modulus of the electric field, as explained in the previous chapter. The resulting signals are linearly combined using the trained output weights to produce the output of the reservoir $y(n)$.

$$y(n) = \sum_{i=1}^N W_i^{\text{out}} |x_i(n)|^2 \quad (3.1)$$

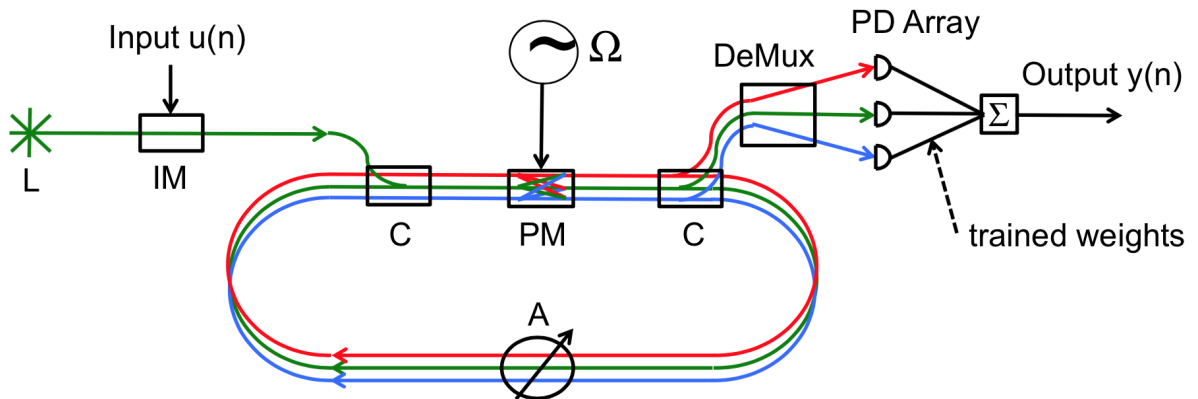


Figure 3.1: Schematic representation of the working principle of the WDM PRC [1]

¹The length of the cavity can be derived from its Free Spectral Range (FSR), which is studied in the next chapter

Training and testing The training scheme used for this setup is the batch learning. Thus, to compute the output weights \mathbf{W}^{out} , one can use the ridge regression technique introduced in section 2.2.2. To do so, one needs to discard the first state vectors \mathbf{x} because they correspond to the transient of the reservoir, and then to store them² as well as the desired outputs \hat{y} during the whole learning period to create the matrices \mathbf{X} and $\hat{\mathbf{Y}}$. After that, it is straightforward to solve equation (2.5) and to find the output weights. Once the RC is trained, it can move on to the testing phase, during which the outputs $y(n)$ are compared to the desired outputs. From that, one can quantify the performance of the RC using the appropriate metric, such as the NMSE for example.

3.1.2 Frequency coupling of the neurons

To mix the different frequencies present inside the reservoir a PM is used. This kind of device is well known for creating equidistant sidebands. Let $Ee^{i\omega t}$ be the input electric field entering the PM. Since a PM is an optoelectronic device, it needs to be externally driven by a voltage generator with a RF modulation signal $V_{\text{RF}}(t) = A \sin(\Omega t)$, with $\Omega \ll \omega$. Using the *Anger-Jacobi* expansion that allows to express the exponential of a trigonometric function in the basis of its harmonics, one can express the effect of a PM:

$$\begin{aligned} Ee^{i\omega t} &\xrightarrow{\Omega} Ee^{i\omega t} e^{im \sin(\Omega t)} \\ &= E \sum_{n=-\infty}^{\infty} J_n(m) e^{i(\omega+n\Omega)t} \end{aligned} \quad (3.2)$$

This formula indicates that the resulting wave is a discrete superposition of planar waves whose frequencies are evenly spaced ($\Omega/2\pi$ between each frequency component) and centred on the input electric field frequency $\omega/2\pi$. The coefficient $J_n(m)$ weighting the superposition is the n^{th} order Bessel function and m is the modulation depth. The latter is related to the modulation amplitude A , but the link between them is not straightforward and is experimentally investigated in the next chapter.

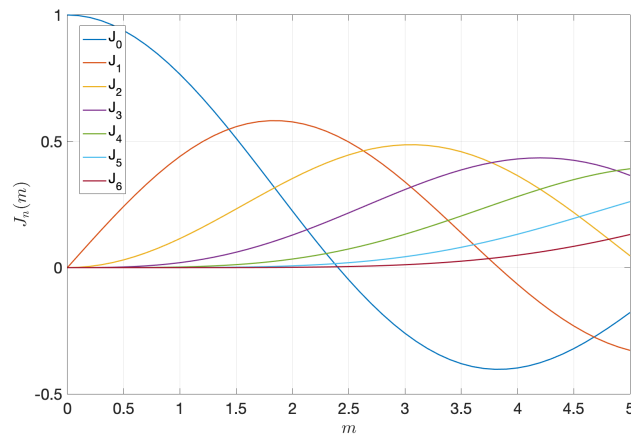


Figure 3.2: Bessel function of order $n \in \{0, \dots, 6\}$

However, what can already be said about m is that it cannot exceed 2 in practice. This is due to the fact that when one increases the modulation frequency $\Omega/2\pi$, the modulation

²Since the output y is constructed using the squared modulus of the activation of the neurons, the matrix \mathbf{X} is filled with $|x_i(n)|^2$ instead of what is indicated in section 2.2.2, namely $x_i(n)$

amplitude A cannot be brought to arbitrarily large values. As a first approximation regarding the RF generator, one could say that the product ΩA is upper bounded. On figure 3.2, one can observe the behaviour the Bessel functions $J_n(m)$ with $n \in \{0, \dots, 6\}$. For $m \in [0, 2]$, $J_n(m)$ becomes less significant for increasing order n . This provides an insight on an intrinsic limitation of this kind of RC, which is the limited number of neurons. A possible solution to improve the scheme would be to use a longitudinal multimode laser³ to inject energy in a wider range of neurons. Yet, the coupling between distant neurons would still be very faint.

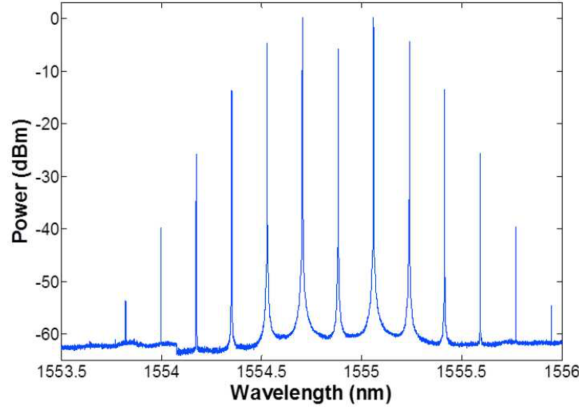


Figure 3.3: Experimental spectral density inside the reservoir [1]

On figure 3.3, the elements regarding the fast decrease of the intensity of the sidebands brought to light in the previous paragraph are confirmed experimentally. On this graph, one can see that only 13 neurons are usable in practice. One also notices that the spectrum is symmetric with respect to the central neuron. This can be explained by the fact that the height of the n^{th} peak is $\propto |J_n(m)|^2$, and by using a property of the Bessel functions that says that for $n \in \mathbb{Z}$, $J_{-n}(m) = (-1)^n J_n(m)$:

$$|J_{-n}(m)|^2 = |(-1)^n J_n(m)|^2 = |J_n(m)|^2 \quad (3.3)$$

3.1.3 Mathematical model

This section tackles the derivation of the discrete equation governing the dynamics of the reservoir. This calculation relies on the result stemming from the previous section regarding the effect of a PM on an incident electric field. As a first step, the state \mathbf{x} is expressed using a convenient formalism. The end goal here is to be able to use linear algebra because it makes the derivation easier. Let N be the total number of neurons. This implies that \mathbf{x} should be a N -dimensional vector that can be developed as a linear combination of basis vectors:

$$\mathbf{x} = \sum_{i=1}^N x_i \hat{\mathbf{e}}_i \quad (3.4)$$

If the basis vectors are adequately chosen, the state vector \mathbf{x} can reduce to the value of the electric field inside the reservoir. The basis vectors are defined as:

$$\hat{\mathbf{e}}_n = e^{i\omega_n t} = e^{i(\omega + n\Omega)t} \quad (3.5)$$

³A longitudinal multimode laser emits light at different frequencies

Moreover, to be consistent, the numbering of the neurons should be modified such that $\hat{\mathbf{e}}_0$ corresponds to the central frequency. Let η be the new variable used to iterate through the neurons such that the sum in the linear combination will go from $-\eta$ to η instead of from 1 to N . η is given by $\lfloor N/2 \rfloor$. The state vector \mathbf{x} now reads:

$$\mathbf{x} = \sum_{i=-\eta}^{\eta} x_i \hat{\mathbf{e}}_i \quad (3.6)$$

This is precisely equal to the electric field inside the reservoir. The results from the previous section can now be used to derive the discrete dynamics equation. Knowing the value of each of the neurons at discrete time n and the effect of a PM, one can compute the new state vector. To do so, linear algebra is used. One knows that the reservoir is linear, therefore, it should be possible to find a linear mapping between two successive states. If there exists a linear mapping, since one is working in discrete space, there is a matrix representation of this mapping. Furthermore, given that one knows the effect of a PM on each of the basis vectors, one can explicitly define this matrix.

$$\mathbf{J} = \begin{bmatrix} J_0(m) & J_{-1}(m) & \dots & J_{-\eta}(m) & \dots & J_{-2\eta} \\ J_1(m) & J_0(m) & \dots & J_{-\eta+1}(m) & \dots & J_{-2\eta+1} \\ \vdots & \vdots & & \vdots & & \vdots \\ J_{2\eta}(m) & J_{2\eta-1}(m) & \dots & J_{\eta}(m) & \dots & J_0 \end{bmatrix} \quad (3.7)$$

One should note that each time the light goes around the cavity, it acquires some phase which is dependent on the wavelength. This should be taken into account in the derivation as well. If ϕ_i is the phase acquired by the neuron propagating with the frequency $\omega_i/2\pi$, one can define the phase matrix:

$$\Phi = \begin{bmatrix} e^{i\phi_{-\eta}} & 0 & \dots & \dots & \dots & 0 \\ 0 & e^{i\phi_{-\eta+1}} & 0 & \dots & \dots & 0 \\ \vdots & 0 & \ddots & & & \vdots \\ \vdots & \vdots & & e^{i\phi_i} & & \vdots \\ \vdots & \vdots & & & \ddots & 0 \\ 0 & 0 & \dots & \dots & 0 & e^{i\phi_{\eta}} \end{bmatrix} \quad (3.8)$$

Both \mathbf{J} and Φ are $N \times N$ matrices, with associated linear operators $\hat{\mathbf{J}}$ and $\hat{\Phi}$. Finally, recalling that α and β are the feedback and input gains, respectively, and that the source laser only injects light in the central wavelength, one can express the discrete time dynamics of the reservoir:

$$\mathbf{x}(n+1) = \alpha \hat{\Phi} \hat{\mathbf{J}} \left(\mathbf{x}(n) + \beta u(n+1) \hat{\mathbf{e}}_0 \right) \quad (3.9)$$

The value of α can be adjusted experimentally by changing the intra-cavity amplification and that of β numerically in the computer controlling the experiment.

Chapter 4

Interferometric stabilisation of reservoir cavity

4.1 Introduction

In this introductory section, the concept of interferometry is presented. As the name of the chapter suggests, this technique is used to stabilise the reservoir cavity. The reason why an optical cavity needs stabilisation will appear clearer later, but basically, this is due to the fact that light is a wave and that it can interfere with itself inside the cavity. The interferences can be constructive, destructive, or can behave in any intermediate way. Moreover, it will be shown that the interferometric properties are wavelength dependent. Since several wavelengths coexist inside the reservoir, this gives a first glimpse on the complexity entailing its stabilisation. To gain some insight on interferometry, and before moving on to the study of an actual ring cavity, the features of the well known Fabry-Perot (FP) interferometer are recalled. After that, it is shown that the properties studied for the FP can be translated to ring cavities with close to no modification. Finally, under the light of the basic notions of interferometry developed, the difficulties linked to the stabilisation of the reservoir cavity, which is at the heart of the scheme introduced in this thesis, are presented.

4.1.1 Fabry-Perot interferometer

The FP plays an important role in modern optics as it is really ubiquitous. This can be explained by the fact that, despite its great simplicity, it can reach good performance using high reflectivity mirrors, which can be produced using nowadays technologies. In practice, a FP cavity is simply made of two facing mirrors as can be viewed on figure 4.1. On this figure, one can see the two mirrors, represented by the vertical black lines, and the different electric fields. The resonance condition, namely the regime where the transmitted electric field E_t is maximum, can be seen intuitively as a situation where the intra-cavity field E_1 is in phase with the incident field E_{in} , which leads to the build up of a very intense intra-cavity electric field. On the other hand, the anti-resonance condition is met when E_{in} and E_1 are out of phase. The transmissivity of the FP interferometer, which is defined as the ratio $|E_t|^2/|E_{in}|^2$, is given by [31]:

$$\mathcal{T}(\omega) = \frac{1}{1 + \mathcal{F} \sin^2\left(\frac{\omega}{\text{FSR}}\right)} \quad (4.1)$$

In this expression, \mathcal{F} is the finesse of the cavity, ω is the angular frequency of the incident electric field, and FSR is the Free Spectral Range of the cavity. In a stationary

regime, the energy inside the cavity does not evolve, therefore the energy carried by the incident electric field E_{in} can either be transmitted or reflected, which implies that the reflectivity of the cavity which is defined as the ratio $|E_{\text{ref}}|^2/|E_{\text{in}}|^2$ is simply given by:

$$\mathcal{R}(\omega) = 1 - \mathcal{T}(\omega) \quad (4.2)$$

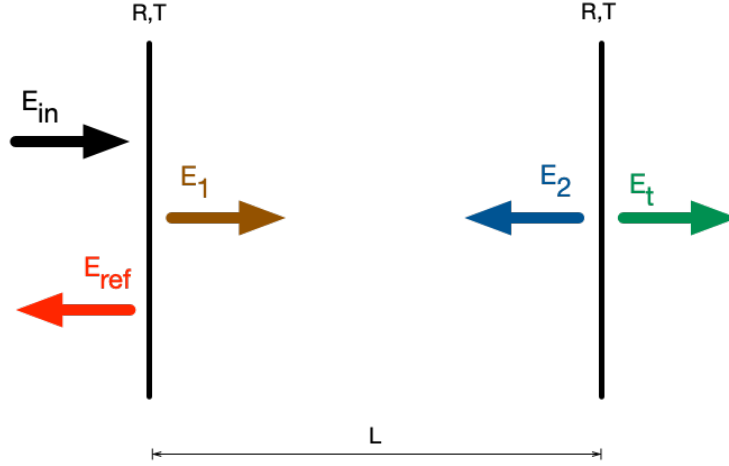


Figure 4.1: Schematic representation of a Fabry-Perot interferometer. E_{in} is the incident electric field, E_{ref} is the reflected electric field, E_t is the transmitted electric field, E_1 is the intra-cavity electric field propagating from left to right, E_2 is the intra-cavity electric field propagating from right to left, R and T are the reflectivity and transmissivity of the mirrors and L is the distance between them.

On figure 4.2, the transmissivity (right) and reflectivity (left) can be viewed. These graphs are made of peaks which are distant of the FSR in the spectral domain. Recalling that $\text{FSR} = c/2nL$, one can see that the FSR is linked to the length of the cavity, with c the speed of light and n the refractive index of the medium that could be present between the two mirrors (nL is the optical path). The finesse \mathcal{F} is related to the width of the peaks and depends on the reflectivity of the mirrors as $\mathcal{F} = 4R/(1 - R)^2$. As the reflectivity of the mirrors tends to 1, the finesse tends to infinity, and the peaks get infinitely narrow. On the other hand, with a lower reflectivity, more energy can leak out of the cavity even outside the resonance condition. Seeing the broadening of the peaks as energy leakage will be useful when drawing a parallel between FP and ring cavity interferometers.

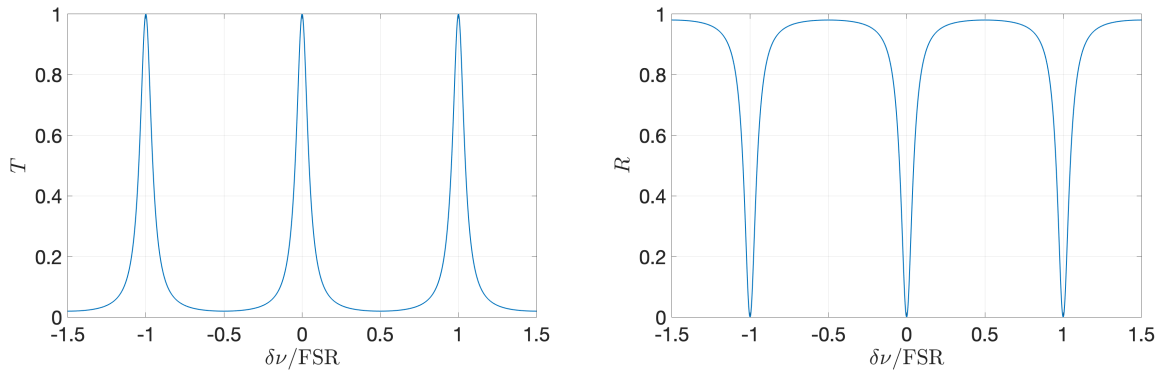


Figure 4.2: Transmissivity \mathcal{T} (left) and reflectivity \mathcal{R} (right) of the cavity. Finesse $\mathcal{F} = 50$. $\delta\nu$ denotes the deviation from a resonant frequency.

Equation (4.1) and (4.2) indicate that \mathcal{T} and \mathcal{R} depend on ω/FSR . This value can be rearranged as:

$$\frac{\omega}{\text{FSR}} = kL = \phi \quad (4.3)$$

Where k is the wave number defined as $n\omega/c$ and ϕ is the phase acquired by the electric field when propagating along the cavity. Therefore, by measuring the transmitted or reflected power, one can gain information about the phase (modulo π , because the periodicity of \mathcal{T} and \mathcal{R} in the phase domain is π) of the electric field. This is the idea underlying interferometry.

4.1.2 Ring cavity

A ring cavity exhibits the same behaviour as a FP interferometer. The structure of a ring cavity interferometer is displayed on figure 4.3. This is a fibre-based setup in which the incident electric field E_{in} penetrates the cavity from the left through a coupler. E_{ref} denotes the electric field exiting the cavity and E_1 and E_2 refer to the fields entering and leaving the fibre loop, respectively. The nomenclature for the fields was chosen in such a way that the analogy with the FP cavity can be understood. Indeed, one could see the coupler acting as the leftmost mirror from the figure 4.1, and the fibre loop as the one on the right side because it turns E_1 into E_2 and dissipates energy through fibre losses, whereas for the mirror it was by leakage out of the cavity.

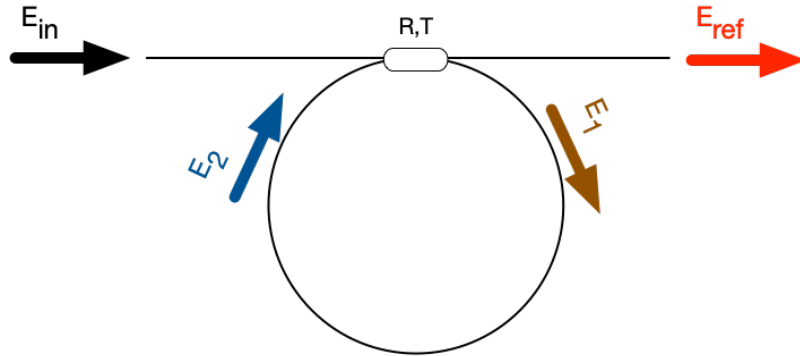


Figure 4.3: Schematic view of a ring cavity

Because of the similarities between ring cavities and FPs, the former show the same transmissivity and reflectivity as the latter. Therefore, by measuring the reflected power, one can determine the phase acquired by the electric field inside the cavity.

4.1.3 Challenge

The basic principle of interferometry has been introduced through the presentation of the FP interferometer, and in the discussion that followed, it has been shown that a ring cavity, such as the reservoir cavity studied in this thesis, can be used as an interferometer. Moreover, it has also been showed that \mathcal{R} depends on the frequency (or wavelength) and on the length of the cavity and that the phase acquired by the incident electric field after one round trip could be determined by studying the reflected power.

In the reservoir cavity, many different wavelengths coexist because they encode the different neurons. Furthermore, after each round trip, the phase acquired by each neuron

should be a constant, as shown on equation (3.9). Recalling the phase matrix Φ defined in equation (3.8), the phase factor multiplying the k^{th} neuron is given by $\Phi_{kk} = \exp(i\phi_k)$. The phase ϕ_k is given by:

$$\phi_k = \beta(\omega + k\Omega)L \quad (4.4)$$

With β the fibre wave number, $\omega + k\Omega$ the angular frequency of the k^{th} neuron and L the length of the fibre loop. Because $k\Omega \ll \omega$, the wave number can be Taylor expanded:

$$\beta(\omega + k\Omega) = \beta(\omega) + \left. \frac{\partial \beta}{\partial \omega} \right|_{\omega} k\Omega + \mathcal{O}((k\Omega)^2) \quad (4.5)$$

By rewriting $\beta(\omega)$ and $\partial\beta/\partial\omega|_{\omega}$ as β_0 and β_1 as it is often done in the literature, the acquired phase is given by:

$$\phi_k \approx \beta_0 L + k\beta_1 \Omega L = \phi_0 + k\phi_1 \quad (4.6)$$

This means that if ϕ_1 is an integer multiple of π , the phase factor multiplying all the neurons will be the same up to a sign:

$$e^{i(\phi_0 + k\phi_1)} = e^{i\phi_0} e^{ikm\pi} = (-1)^{km} e^{i\phi_0}, \quad m \in \mathbb{Z} \quad (4.7)$$

A periodicity of π and not 2π is considered here, because as claimed before, an interferometer can only inform about a phase modulo π . Looking for an acquired phase equal to π is the approximately the same as taking a modulation frequency Ω for the PM which is an integer multiple of the FSR. Indeed, by considering $\beta_1 \approx n/c$, one can find:

$$\beta_1 \Omega L \approx \frac{\Omega n L}{c} = m\pi \longrightarrow \Omega \approx \frac{m\pi c}{nL} = m2\pi \text{ FSR} \quad (4.8)$$

This is a legitimate assumption given the fact that in the region of interest the curve of $\beta(\omega)$ computed using the Sellmeier relations [6, 25] is very linear.

It is not critical to modulate the phase at an angular frequency Ω which is an integer multiple of the FSR, the reservoir can in fact operate in different regimes. Those considerations were presented to better understand the physics underlying the phase management of the reservoir.

The main practical challenge regarding the reservoir concerns its stabilisation. The reservoir has to be stabilised because during its operation, external elements disturb it, which deteriorates the performances and even make it unusable in the worst case. The perturbations acting on the reservoir can come from various sources, such as mechanical constraints or temperature changes for example, and can induce a phase fluctuation. This is where interferometric stabilisation comes into play. Indeed, by measuring the power reflected by the reservoir, one can infer the current phase and take the appropriate action to maintain it at a setpoint. This can be achieved using classical regulation strategies, such as a Proportional-Integral-Derivative (PID) regulator. Elements of regulation will be presented later. Furthermore, this needs to be performed for all the neurons at the same time. This explains why different elements regarding the relative phases between the different neurons were discussed in the previous paragraph. Finally, the last technological difficulty associated to this scheme is the fact that the electric field used to stabilise the cavity is modulated in amplitude to carry the data to be processed by the reservoir. Indeed, a regulator struggles to differentiate a variation in the reflected power due to a phase fluctuation or to the modulation of the incident field.

4.2 Experimental setup

In this section, the experimental setup employed to physically implement the WDM PRC is presented. First, it is detailed based with the help of the schematic representation of figure 4.4. Then, technical data about the devices involved in the experiment are given.

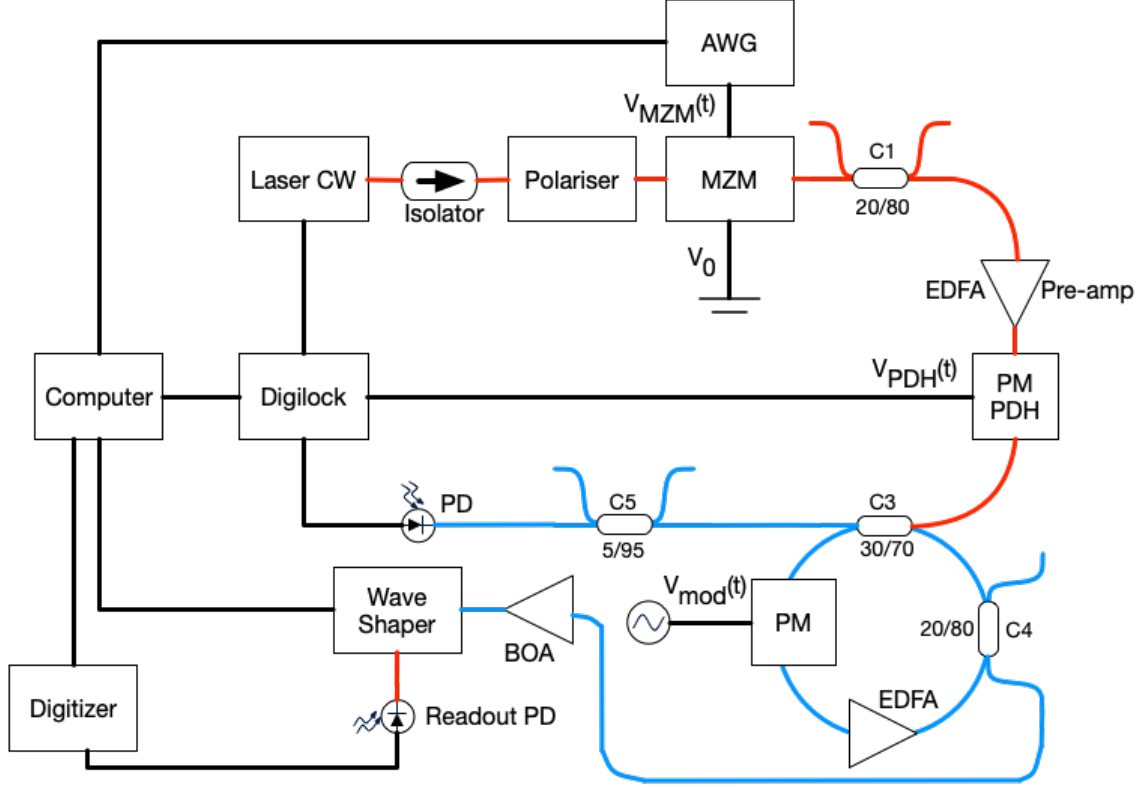


Figure 4.4: Schematic representation of the experimental setup for the WDM reservoir computer experiment

The setup presented here is mostly an update on the one presented on [1]. On figure 4.4, electrical wires and single mode polarisation maintaining fibres are represented using black and coloured lines, respectively. The light source exciting the setup is a narrow band continuous laser, which sends a single wavelength $\lambda_0 = 1555$ nm to the reservoir. The light goes through an isolator that prevents any backward reflection towards the laser source and then enters a polariser that ensures that only one linear polarisation mode is present inside the setup. This needs to be done because the optoelectronic devices involved in the experiment, such as the MZM and the PMs, are polarisation dependent. The electric field then enters a MZM which is driven by the time dependent voltage $V_{\text{MZM}}(t)$. This signal is generated by an Arbitrary Wave Generator (AWG) based on the input time series $u(n)$ sent by the computer running the experiment. Since the transfer function of the MZM is nonlinear, the signal V_{MZM} can be precompensated in order to counteract the nonlinearity. Without precompensation, the voltage $V_{\text{MZM}}(t)$ is simply given by $\beta \tilde{u}(t)$, with β the input gain $\in [0, 1]$ and $\tilde{u}(t)$ the *sample and hold* version of $u(n)$ already introduced in the previous chapter. A bias tension V_0 can also be applied to the MZM to change its average transparency. The transfer function of the MZM is given by :

$$\sin \left(\frac{\pi}{2} \left(\frac{V_{\text{MZM}}(t)}{V_{\pi, \text{RF}}} + \frac{V_0}{V_{\pi, \text{DC}}} \right) \right) \quad (4.9)$$

With $V_{\text{MZM}} \in [-\beta V_{\pi,\text{RF}}, \beta V_{\pi,\text{RF}}]$, and $V_{\pi,\text{RF}}$ and $V_{\pi,\text{DC}}$ the dynamic and static characteristic voltages of the MZM, respectively. The modulated electric field is then pre-amplified using an Erbium-Doped Fibre Amplifier (EDFA), and undergoes a first phase modulation. This is required to be able to implement the Pound-Drever-Hall (PDH) stabilisation technique, which is an advanced cavity stabilisation scheme that is described with greater length in section 4.4. The PM is driven by the alternative voltage $V_{\text{PDH}} = A_{\text{PDH}} \sin(\Omega_{\text{PDH}} t)$ supplied by the *Toptica Digilock 110* feedback controller denoted "Digilock" on the figure. This device handles every aspects related to the stabilisation of the reservoir, which is why it needs to be connected to the photodiode "PD" and to the laser, which are both involved in the regulation of the cavity (see later). The electric field then enters the reservoir through the coupler "C3". The reservoir cavity is made of the fibres of the different couplers and is around 18m long. At this point, the colour used to represent the optical fibres changes from red to blue to indicate that inside the reservoir, several wavelengths are present whereas before the coupler there was only one. Inside the reservoir, the PM is used to mix the different frequencies and is driven by an external alternative voltage $V_{\text{mod}}(t) = A_{\text{mod}} \sin(\Omega_{\text{mod}} t)$. To allow a clear distinction between the different sidebands without degrading the achievable modulation depth, the modulation frequency $\Omega_{\text{mod}}/2\pi$ is around 20 GHz. This allows the existence of 13 neurons inside the cavity (6 sidebands on both sides of the central frequency) with wavelengths going from $1.554 \mu\text{m}$ to $1.556 \mu\text{m}$. The PM introduces insertion losses that are compensated using the EDFA, whose pump current is adjusted to tune the feedback gain α that appears in equation (3.9). The electric field exiting the reservoir at the level of the coupler "C3" towards the photodiode "PD" is the reflected field, according to what was discussed in section 4.1.2. The electric field finally illuminates the photodiode "PD", which produces a voltage proportional to its intensity. This measured signal enters the Digilock where it is compared to a reference. Based on the deviation between those two values, the Digilock outputs a control voltage that is applied to a piezoelectric crystal inside the laser cavity and that modifies its emission wavelength. The output of the reservoir exits the cavity through the coupler "C4" and is amplified by a SOA called "BOA" for Boost Optical Amplifier to improve the SNR. A demultiplexing scheme allowing to obtain the value of each individual neuron at the same time has not been implemented yet. To overcome this limitation, the adjustable band-pass filter denoted "Wave Shaper" is used to record the evolution of only one neuron at a time. This implies that if one wants to compute the output of the reservoir $y(n)$, one has to run the same experiment once for each of the neuron, to program the Wave Shaper to filter out all the other sidebands and to save its evolution on the computer. Once this has been done, $y(n)$ can be reconstructed. As far as the learning procedure is concerned, it follows the same procedure as the one previously described, but modified to take this sequential measurements of the neurons into account. In terms of the devices used to perform this task, the photodiode "Readout PD" measures the intensity of each of the filtered neuron, and the "Digitizer" handles the conversion between continuous time dependent signals into time series usable by the computer. To conclude this description of the experimental setup, one should note that even though the couplers "C1" and "C2" seem useless, they are used in practice to monitor the electric fields when modifications are made to the optical table, and that the AWG, Digilock, Wave Shaper and Digitizer are all controlled by the computer. The technical specifications of the devices used in the experiment can be found in appendix B.

4.3 Characterisation of the reservoir

To be able to develop a reliable stabilisation scheme for the reservoir, some of its characteristics need to be studied as a preliminary work. First, one can gain important insights by modelling the transfer function of the reservoir. In this context, the transfer function is simply the reflectivity of the cavity. However, given the fact that the reservoir is a more complex ring cavity than the one depicted in section 4.1.2, it will not exhibit the exact same behaviour as the one of a FP cavity as displayed on figure 4.2. A mathematical model is first derived and the results it provides are compared to experimental transfer functions. After that, the experimental study of the effective losses is tackled. The effective losses are used in the model to take into account the fibre losses, the insertion losses of the PM and the gain of EDFA using only one factor. Finally, an empirical relation between the modulation amplitude driving the intra-cavity PM and its modulation depth is determined experimentally.

4.3.1 Transfer function of the cavity

As already claimed, in the context of cavity stabilisation, the transfer function is the reflectivity. When operating the reservoir, the reflected power which is proportional to the intensity of the electric field reflected by the cavity gives an indication on the phase of the field inside it, which implies that the regulation procedure relies on the measurement of this signal.

On figure 4.5, the reservoir is represented with the different electric fields that turn out to be useful when studying the transfer function. The colour code for the fibres is the same as the one used previously. The incident electric field \mathbf{E}_{in} enters the cavity through a coupler from the top left optical fibre. Inside the cavity, it is amplified by the EDFA and then is phase modulated. After that, a portion of the electric field exits the cavity through the coupler C4 to be read out. The light inside the cavity finally terminates its round trip.

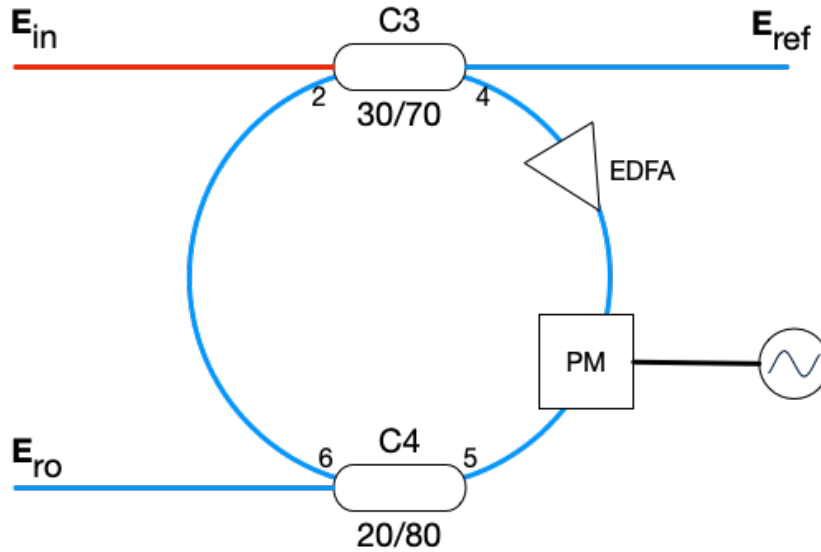


Figure 4.5: Schematic representation of the reservoir

Mathematical model

In this section, a mathematical model for the transfer function is derived. To do so, the formalism introduced in section 3.1.3 needs to be used. This can be done because the basis vectors were chosen such that a neuron's state vector \mathbf{x} is formally equal to an electric field. Therefore, one should pay attention to the fact that when referring to a vectorial electric field \mathbf{E} , it denotes an electric field expressed in the abstract basis $\{\hat{\mathbf{e}}_j | \hat{\mathbf{e}}_j = \exp(i(\omega + j\Omega_{\text{mod}}t)), j \in [-\eta, \eta]\}$ instead of the usual physical space $\{\mathbf{1}_x, \mathbf{1}_y, \mathbf{1}_z\}$.

The transfer function \mathbf{R} is defined as the link between the incident and reflected electric fields:

$$\mathbf{E}_{\text{ref}} = \mathbf{R} \mathbf{E}_{\text{in}} \quad (4.10)$$

Given the vectorial nature of \mathbf{E}_{ref} and \mathbf{E}_{in} , the transfer function is in fact a transfer matrix in this particular context. Recalling that the laser only emits light at the center wavelength, the incident field \mathbf{E}_{in} is given by:

$$\mathbf{E}_{\text{in}} = E_0 \hat{\mathbf{e}}_0 \quad (4.11)$$

With E_0 being an arbitrary complex amplitude. Given the properties of the coupler C3, one finds:

$$\begin{bmatrix} \mathbf{E}_{\text{ref}} \\ \mathbf{E}_4 \end{bmatrix} = \begin{bmatrix} \varepsilon_1 & i\sqrt{1-\varepsilon_1^2} \\ i\sqrt{1-\varepsilon_1^2} & \varepsilon_1 \end{bmatrix} \begin{bmatrix} \mathbf{E}_{\text{in}} \\ \mathbf{E}_2 \end{bmatrix} \quad (4.12)$$

Which yields to the following expression for the reflected field:

$$\mathbf{E}_{\text{ref}} = \varepsilon_1 \mathbf{E}_{\text{in}} + i\sqrt{1-\varepsilon_1^2} \mathbf{E}_2 \quad (4.13)$$

Let us now express \mathbf{E}_2 as a function of \mathbf{E}_{in} to close the system. Using the transfer matrix of the coupler C4, \mathbf{E}_2 reads :

$$\begin{bmatrix} \mathbf{E}_2 \\ \mathbf{E}_{\text{ro}} \end{bmatrix} = e^{-\gamma L} \begin{bmatrix} \varepsilon_2 \\ \sqrt{1-\varepsilon_2^2} \end{bmatrix} \mathbf{E}_5 \implies \mathbf{E}_2 = \varepsilon_2 e^{-\gamma L} \mathbf{E}_5 \quad (4.14)$$

With γ the effective losses coefficient and L , the length of the reservoir. Since the system is in a linear regime, the position of the coupler C4 in the cavity has no influence on the losses and on the phase. By defining $\xi \in [0, 1]$ as the variable indicating the relative position of the PM inside the cavity ($\xi = 0$ if it is at the beginning of the cavity, $\xi = 1$ if it is at the end). The phase acquired by the electric field inside the reservoir is now dependent on the position of the PM. This leads to the definition of two new matrices Φ_ξ and $\Phi_{1-\xi}$, which are based on the phase matrix Φ . They are diagonal matrices, expressed as:

$$\begin{aligned} \Phi_{\xi,nn} &= \exp(i\beta(\omega + n\Omega_{\text{mod}})\xi L) \\ \Phi_{1-\xi,nn} &= \exp(i\beta(\omega + n\Omega_{\text{mod}})(1-\xi)L) \end{aligned} \quad (4.15)$$

With $\beta(\omega + n\Omega_{\text{mod}})$ the dispersion relation of the fibre evaluated at the frequency of the n^{th} neuron. Recalling the coupling matrix of the PM \mathbf{J} , one can rewrite \mathbf{E}_5 as a function of \mathbf{E}_4 :

$$\mathbf{E}_5 = \Phi_{1-\xi} \mathbf{J} \Phi_\xi \mathbf{E}_4 \quad (4.16)$$

Using the transfer matrix of the coupler C3, one can express \mathbf{E}_4 as a function of \mathbf{E}_{in} and \mathbf{E}_2 :

$$\mathbf{E}_4 = i\sqrt{1 - \varepsilon_1^2} \mathbf{E}_{\text{in}} + \varepsilon_1 \mathbf{E}_2 \quad (4.17)$$

This yields to a closed equation to determine \mathbf{E}_2 :

$$\begin{aligned} \mathbf{E}_2 &= i\sqrt{1 - \varepsilon_1^2} \varepsilon_2 e^{-\gamma L} \Phi_{1-\xi} \mathbf{J} \Phi_\xi \mathbf{E}_{\text{in}} + \varepsilon_1 \varepsilon_2 e^{-\gamma L} \Phi_{1-\xi} \mathbf{J} \Phi_\xi \mathbf{E}_2 \\ \hookrightarrow \mathbf{E}_2 &= i\sqrt{1 - \varepsilon_1^2} \varepsilon_2 e^{-\gamma L} (\mathbf{I} - \varepsilon_1 \varepsilon_2 e^{-\gamma L} \Phi_{1-\xi} \mathbf{J} \Phi_\xi)^{-1} \Phi_{1-\xi} \mathbf{J} \Phi_\xi \mathbf{E}_{\text{in}} \end{aligned} \quad (4.18)$$

Now that \mathbf{E}_2 has been determined, it is easy to compute \mathbf{E}_{ref} using equation (4.13):

$$\begin{aligned} \mathbf{E}_{\text{ref}} &= \varepsilon_1 \mathbf{E}_{\text{in}} - (1 - \varepsilon_1^2) \varepsilon_2 e^{-\gamma L} (\mathbf{I} - \varepsilon_1 \varepsilon_2 e^{-\gamma L} \Phi_{1-\xi} \mathbf{J} \Phi_\xi)^{-1} \Phi_{1-\xi} \mathbf{J} \Phi_\xi \mathbf{E}_{\text{in}} \\ \hookrightarrow \mathbf{E}_{\text{ref}} &= (\varepsilon_1 \mathbf{I} - (1 - \varepsilon_1^2) \varepsilon_2 e^{-\gamma L} (\mathbf{I} - \varepsilon_1 \varepsilon_2 e^{-\gamma L} \Phi_{1-\xi} \mathbf{J} \Phi_\xi)^{-1} \Phi_{1-\xi} \mathbf{J} \Phi_\xi) \mathbf{E}_{\text{in}} \end{aligned} \quad (4.19)$$

This last equality reveals the expression of the transfer matrix \mathbf{R} :

$$\boxed{\mathbf{R} = \varepsilon_1 \mathbf{I} - (1 - \varepsilon_1^2) \varepsilon_2 e^{-\gamma L} (\mathbf{I} - \varepsilon_1 \varepsilon_2 e^{-\gamma L} \Phi_{1-\xi} \mathbf{J} \Phi_\xi)^{-1} \Phi_{1-\xi} \mathbf{J} \Phi_\xi} \quad (4.20)$$

Even if this result is interesting, it cannot be measured directly since it involves electric fields instead of intensities. What is measured using a PD is the reflectivity \mathcal{R} linking the incident intensity to the reflected intensity. Recalling that the incident electric field is given by $\mathbf{E}_{\text{in}} = E_0 \hat{\mathbf{e}}_0$, the reflected electric field is given by:

$$\mathbf{E}_{\text{ref}} = \mathbf{R} \mathbf{E}_{\text{in}} = E_0 \sum_{n=-\eta}^{\eta} R_{n,0} \hat{\mathbf{e}}_n \quad (4.21)$$

The sum in this formula is expressed using the numbering introduced in section 3.1.3 which is more natural for this kind of situation. As a reminder, instead of going through the indices from 1 to N , this alternative notation goes from $-\eta$ to η , with index 0 referring to the central neuron. Thus, the above equation basically means that \mathbf{E}_{ref} is equal to E_0 multiplying the central column of \mathbf{R} .

The reflected intensity is given by:

$$|\mathbf{E}_{\text{ref}}|^2 = |E_0|^2 \left(\sum_{n=-\eta}^{\eta} R_{n,0} \hat{\mathbf{e}}_n \right) \left(\sum_{m=-\eta}^{\eta} R_{m,0}^* \hat{\mathbf{e}}_m^* \right) \quad (4.22)$$

This expression seems complicated at first sight, but it can be simplified by putting forward an experimental argument. First, let us consider the product $\hat{\mathbf{e}}_n \cdot \hat{\mathbf{e}}_m^*$, which is equal to $\exp(i(n-m)\Omega_{\text{mod}}t)$. If $m = n$, then the product is equal to one and the term $|R_{n,0}|^2$ has to be taken into account in the sum. On the other hand, if $m \neq n$, then product corresponds to a beating of the intensity at frequency $(n-m)\Omega_{\text{mod}}/2\pi$, which is an integer number of times approximately 20 GHz. However, as can be seen in the appendix B, the bandwidth of the PD is limited to 120 MHz. Therefore the PD is not able to resolve the beating waves, which implies that when $m = n$, the signals do not contribute to the sum. This yields to a simplified version of the reflected intensity:

$$|\mathbf{E}_{\text{ref}}|^2 = |E_0|^2 \sum_{n=-\eta}^{\eta} |R_{n,0}|^2 \quad (4.23)$$

The reflectivity of the reservoir is finally given by:

$$\mathcal{R} = \sum_{n=-\eta}^{\eta} |R_{n,0}|^2 \quad (4.24)$$

Note that this model is solely valid when considering the evolution of the reservoir at time scales much larger than $2\pi/\omega$. This assumption ensures that one is working in a stationary regime with respect to the oscillations of the electric field.

Experimental results

The adequacy of the analytical model just derived is assessed by comparing its predictions to experimental data. To capture data concerning transfer functions, one performs a *sweep* using the Digilock. As already explained, the Digilock is connected to a piezoelectric crystal controlling the emission wavelength of the laser, whose shift is proportional to the applied tension. As a reminder, the transfer function is the reflectivity \mathcal{R} as a function of ω , therefore one needs to be able to scan the frequency domain. The sweep procedure allows to do it by applying a triangular periodic voltage to the piezoelectric, which leads to a similar evolution of the emission wavelength of the laser. The frequency and amplitude of this signal are controlled by the Digilock interface. After doing this trick, one can plot the reflected power as a function of the time to observe its shape.

To relate the theoretical curves to raw data, one should express the link between the time and the angular frequency. Using a first order Taylor approximation, the angular frequency variation reads:

$$\delta\omega = -\frac{2\pi c}{\lambda_0^2} \delta\lambda \quad (4.25)$$

With λ_0 the central wavelength (1555 nm). In appendix B, one can find that the piezoelectric tuning characteristic is equal 0.1 pm/V at a sweeping frequency of 100 Hz. Let us denote this value by α and let us call β the slope of the triangular voltage as a function of the time, which depends on the settings of the sweep. Multiplying those two constants provides a proportionality indicating the range of wavelengths spanned per unit of time. This yields to a link between time and angular frequency:

$$\omega = -\alpha\beta\frac{2\pi c}{\lambda_0^2}t \quad (4.26)$$

Below, comparisons between simulations and experimental data are shown for three different regimes. Since the theoretical reflectivity \mathcal{R} is a ratio, it is comprised between 0 and 1. Therefore, it had to be rescaled in order to be compared with the reflected powers measured by the PD.

First sideband at resonance If the central neuron is at resonance, this means that Ω_{mod} is chosen such that the first sideband is at resonance as well. In other words, $\Omega_{\text{mod}}/2\pi$ is an integer number of times the FSR of the cavity. This is displayed on figure 4.6.

First sideband halfway between resonance and anti-resonance Ω_{mod} is tuned such that $\Omega_{\text{mod}}/2\pi$ is an odd number of times the quarter of the FSR. The experimental results are given on the figure 4.7.

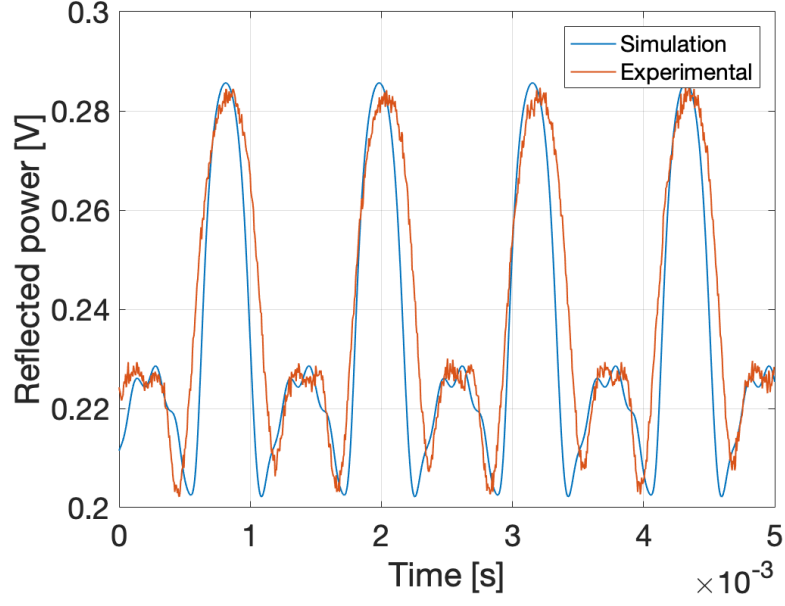


Figure 4.6: Reflected power [V] as a function of the time [s] during a sweep of the Digilock. First sideband at resonance. $\Omega_{\text{mod}} = 19.99$ GHz, modulation depth $m = 2$, $\gamma = 0.0126 \text{ m}^{-1}$

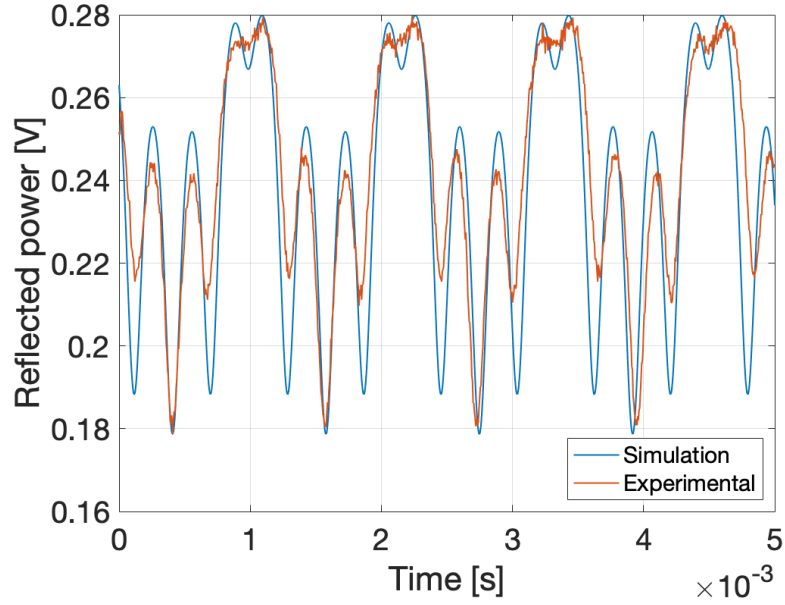


Figure 4.7: Reflected power [V] as a function of the time [s] during a sweep of the Digilock. First sideband halfway between resonance and anti-resonance. $\Omega_{\text{mod}} = 19.9997$ GHz, modulation depth $m = 2$, $\gamma = 0.0126 \text{ m}^{-1}$.

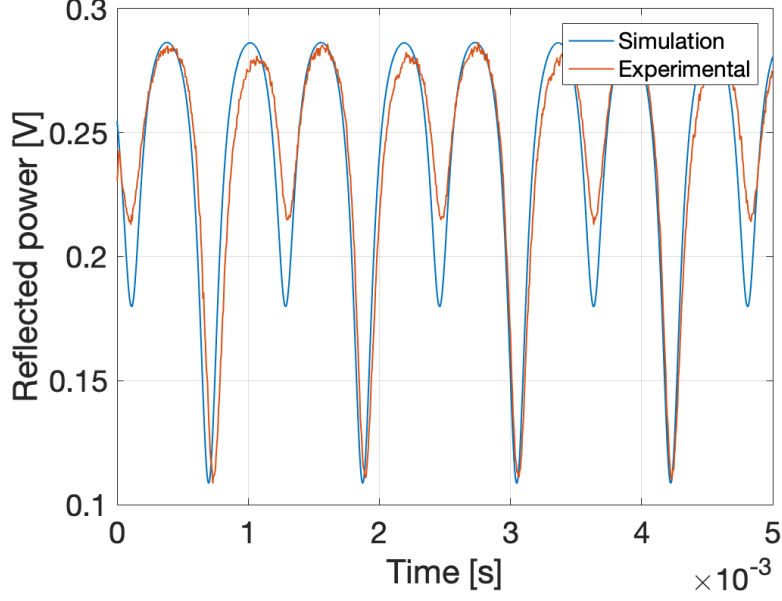


Figure 4.8: Reflected power [V] as a function of the time [s] during a sweep of the Digilock. First sideband at anti-resonance. $\Omega_{\text{mod}} = 19.9997$ GHz, modulation depth $m = 2$, $\gamma = 0.0126 \text{ m}^{-1}$.

First sideband at anti-resonance $\Omega_{\text{mod}}/2\pi$ is an odd number of times half of the FSR. The graphs are depicted on the figure 4.8.

One those graphs, one can see that the transfer function highly depends on the modulation frequency, and more specifically, on the position of the first sideband. Even though the experimental adequacy is not perfect, it is sufficient to have a qualitative idea of the behaviour of the reservoir. It also allows to experimentally deduce its FSR by measuring the temporal periodicity of the reflectivity, and then to translate in the frequency domain using equation (4.26).

$$\Delta t = 1.155 \text{ ms} \implies \text{FSR} \approx \alpha\beta \frac{c}{\lambda_0^2} \Delta t \approx 11.5 \text{ MHz} \quad (4.27)$$

Recalling that the FSR for a ring cavity is given by¹:

$$\text{FSR} = \frac{c}{nL} \quad (4.28)$$

Using this formula, one can compute the length of the cavity: $L = 18.33 \text{ m}$.

As a final remark, the relative position of the PM inside the cavity (controlled using the variable ξ) does not seem to have an influence on the shape of the transfer function.

4.3.2 Effective losses

Given the model derived, the only physical quantity that cannot be known from a simple inspection of the data sheets are the effective losses γ . They arise due to the conjugated effects of the fibre losses, the insertion loss of the intra-cavity PM and the gain of the EDFA, and in the same way that the use of a lower reflectivity mirror induced a worse finesse for a FP, the effective losses lead to a broadening of the resonance peaks.

¹This comes from the fact that the resonance condition is not exactly the same as FP for a ring cavity: $\beta L = 2m\pi$ instead of $\beta L = m\pi$ for a FP

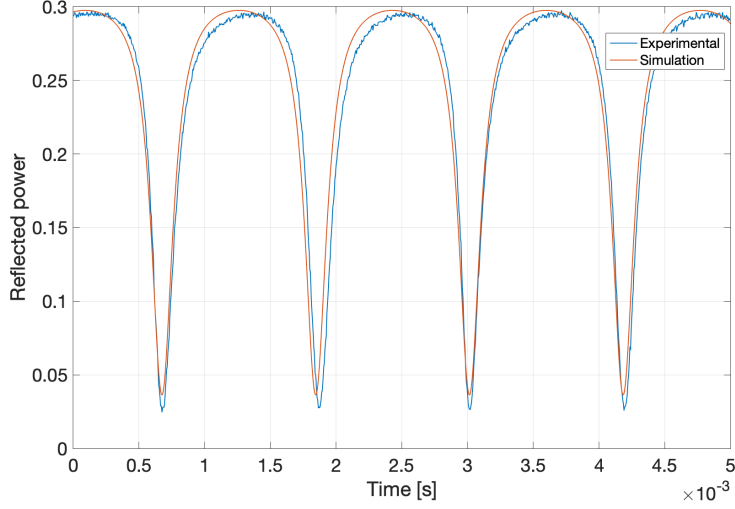


Figure 4.9: Reflected power [V] as function of the time [s] during a sweep of the Digilock, no intra-cavity phase modulation, $\gamma = 0.0126 \text{ m}^{-1}$.

Although their value could have been derived analytically, it has been chosen to determine it experimentally. To do so, a least square fit is performed. Basically, this means that one compares an experimental curve with an analytical one, for which the value of γ is not fixed. The deviation between those two curves is therefore a function of γ , and can be minimised. Mathematically speaking, the experimental effective losses $\tilde{\gamma}$ are given by:

$$\tilde{\gamma} = \underset{\gamma}{\operatorname{argmin}} \sum_{i=1}^T (\mathcal{R}_i - \mathcal{R}(t_i; \gamma))^2 \quad (4.29)$$

Where T is the total number samples, \mathcal{R}_i is the measured reflected power for the i^{th} sample and $\mathcal{R}(t_i; \gamma)$ is the theoretical rescaled reflectivity evaluated at $t = t_i$ and γ , which is the time corresponding to the i^{th} sample and the effective losses, respectively. On figure 4.9, one can see the result of this optimisation. It was performed on the reservoir without phase modulation because it is assumed that the insertion losses do not depend on whether a phase modulation is going on. The effective losses that were determined using this procedure read:

$$\gamma = 0.0126 \text{ m}^{-1} \quad (4.30)$$

4.3.3 Modulation depth

When one wants to modify the modulation depth during a phase modulation process, one has to change the modulation power of the RF generator. However, these two quantities are not the same, even though they are related. The goal of this section is to determine an empirical relation linking the modulation power, expressed in dBm, and the modulation depth. The procedure to compute it is the following: one applies a methodology similar to the one from the previous chapter, except that instead of optimising for γ , one should do it for m , the modulation depth. This procedure is repeated several times, for different modulation powers, in order to form a data set. Finally, when one has gathered enough data, one can perform a polynomial interpolation that provides the link between the power and the depth that one was looking for. This method works better when one is working in the situation where the first sideband is at anti-resonance, because in this this

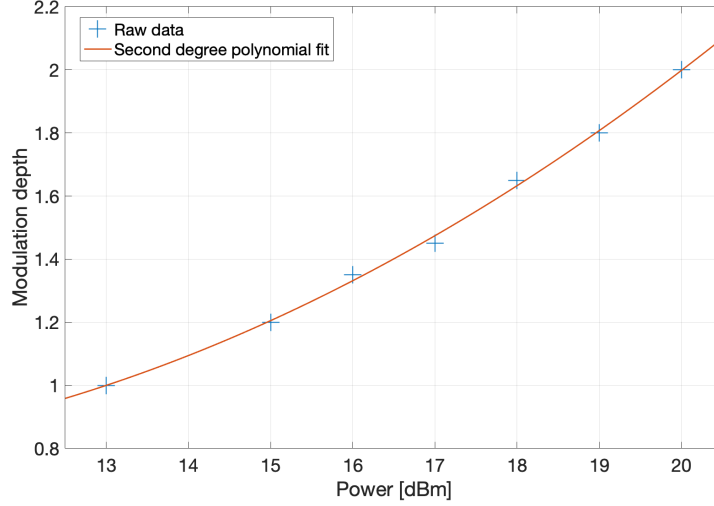


Figure 4.10: Modulation depth m as a function of the modulation power [dBm] and second degree polynomial interpolation for $\Omega_{\text{mod}}/2\pi = 19.9943$ GHz

regime, the depth of the side peaks (see figure 4.8) depends a lot on the modulation depth.

On figure 4.10, one can see the data, as well as the second degree polynomial interpolation. The experimental points only start at 13 dBm because below this value, the side peak was too small to lead significant measures. As already claimed, one cannot go above $m = 2$ experimentally because the RF generator is not able to supply modulation powers higher than 20 dBm at such high modulation frequencies. The empirical polynomial relation is:

$$m(P[\text{dBm}]) = 8.004 \times 10^{-3} P^2[\text{dBm}] - 0.1215 P[\text{dBm}] + 1.222 \quad (4.31)$$

It was decided not to go further that a second degree polynomial interpolation because the results were already satisfying.

4.4 Pound-Drever-Hall stabilisation technique

In this section, the PDH stabilisation technique is presented. First, the rationale behind its introduction is discussed. After that, it is shown that the error function resulting from the PDH modulation reveals new informations about the phase of the electric field inside the cavity that allow to reach better stabilisation performances. Finally, a few remarks are given regarding the implementation of this scheme for the reservoir cavity.

4.4.1 Introduction

The PDH stabilisation technique was proposed in 1983 in [12] and since then has proven to be a powerful scheme enabling to accurately stabilise optical cavities. Among other applications, it has been used to stabilise the laser and measure the thermal noise in the arms of the Michelson interferometer of the LIGO [5], which made possible the observation of gravitational waves.

The basic idea of the PDH technique is to modify the transfer function of the cavity in such a way that its observation will provide more information about the phase. This is

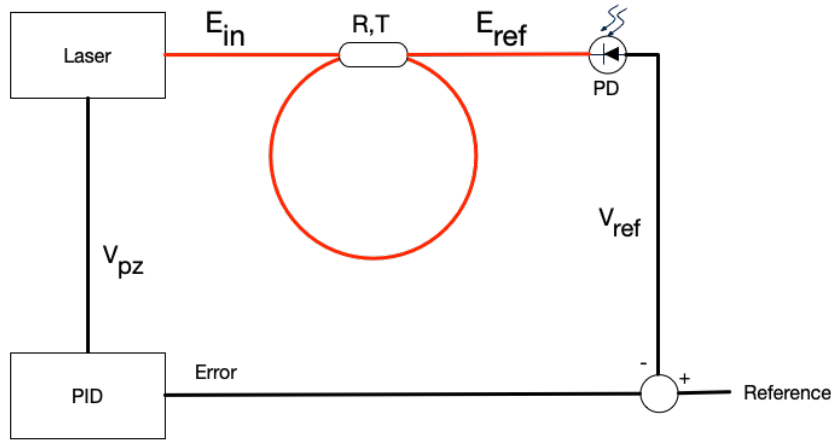


Figure 4.11: Schematic representation of cavity stabilisation

implemented in practice by using an additional PM and some electronic post-processing, which is handled by the Digilock in our setup.

Cavity stabilisation

Before discussing the PDH scheme, the principles of cavity stabilisation are presented. As a reminder, this action consists in keeping the relative phase between the electric field inside the cavity after a round trip and the incident electric field equal to a given reference value. Its value can be estimated by measuring the power reflected by the cavity, and can be modified by using actuators to change either the length of the cavity, or the emission wavelength of the laser.

On figure 4.11, one can observe the basic principle of the regulation of an optical cavity. The top branch of the figure is well-known at this point. The incident field E_{in} enters the cavity at the level of the coupler, where the reflected E_{ref} exits the cavity. The latter is then measured by the PD. Henceforth, the different elements should be looked at under the light of control theory. The measured tension V_{ref} is compared to a reference, which is the value that the regulator is trying to maintain. The difference between the reference and the measured tension is the so-called error, which is processed by a device named the PID regulator. In all generality, a PID regulator, or PID in short, is governed by this equation in the time domain [15, p.196]:

$$u(t) = k_P e(t) + k_I \int_{-\infty}^t e(\tau) d\tau + k_D \frac{de}{dt}(t) \quad (4.32)$$

With $u(t)$ the output of the PID, which is in this context the tension applied to the piezoelectric V_{pz} , $e(t)$ the error and k_I , k_P and k_D the proportional, integral, and differential coefficients, respectively. In order to get the PID to work, one needs to tune those three coefficients, either using analytical methods, or heuristically by scanning the different values. The latter option was the one followed in the experimental implementations described in this work.

The voltage V_{pz} , the output of the PID, is applied to the piezoelectric crystal of the laser and alters its emission wavelength to stay synchronised with the reference.

The main limitation of this scheme is linked to the symmetry of the transfer function \mathcal{R} . Let us illustrate why the symmetry is a shortcoming by considering a specific situation,

The PDH stabilisation technique relies on the addition of a PM and electronic post-processing, as can be viewed on figure 4.13. The light sent by the laser goes through a PM driven by an AC voltage at frequency $\Omega_{\text{PDH}}/2\pi$ emitted by a RF generator. The modulation depth is chosen in such a way that all the sidebands but the first are negligible (one sideband on each side of the carrier frequency). Therefore, the electric field incident on the cavity E_{in} reads:

$$E_{\text{in}} = E_0 (J_0(m)e^{i\omega t} + J_1(m)e^{i(\omega+\Omega_{\text{PDH}})t} - J_1(m)e^{i(\omega-\Omega_{\text{PDH}})t}) \quad (4.33)$$

Given the fact that the cavity is linear, one can assume that its transfer function² R is linear as well, which gives for the reflected field E_{ref} :

$$E_{\text{ref}} = E_0 (J_0(m)R(\omega)e^{i\omega t} + J_1(m)R(\omega + \Omega_{\text{PDH}})e^{i(\omega+\Omega_{\text{PDH}})t} - J_1(m)R(\omega - \Omega_{\text{PDH}})e^{i(\omega-\Omega_{\text{PDH}})t}) \quad (4.34)$$

The voltage at the PD is proportional to the intensity:

$$\begin{aligned} V_{\text{ref}} \propto |E_0|^2 & \left(J_0^2(m)\mathcal{R}(\omega) + J_1^2(m)(\mathcal{R}(\omega + \Omega_{\text{PDH}}) + \mathcal{R}(\omega - \Omega_{\text{PDH}})) \right. \\ & + 2J_0(m)J_1(m)\text{Re}[R(\omega)R^*(\omega + \Omega_{\text{PDH}}) - R^*(\omega)R(\omega - \Omega_{\text{PDH}})] \cos(\Omega_{\text{PDH}}t) \\ & + 2J_0(m)J_1(m)\text{Im}[R(\omega)R^*(\omega + \Omega_{\text{PDH}}) - R^*(\omega)R(\omega - \Omega_{\text{PDH}})] \sin(\Omega_{\text{PDH}}t) \\ & \left. + \text{terms at } 2\Omega_{\text{PDH}} \right) \end{aligned} \quad (4.35)$$

This signal goes to a band pass filter centred at Ω_{PDH} in order to remove the DC component and the terms oscillating at $2\Omega_{\text{PDH}}$. Let us define $\zeta(\omega)$ as:

$$\zeta(\omega) = R(\omega)R^*(\omega + \Omega_{\text{PDH}}) - R^*(\omega)R(\omega - \Omega_{\text{PDH}}) \quad (4.36)$$

The voltage at the output of the band pass filter reads:

$$V_{\text{BP}} \propto \text{Re}[\zeta(\omega)] \cos(\Omega_{\text{PDH}}t) + \text{Im}[\zeta(\omega)] \sin(\Omega_{\text{PDH}}t) \quad (4.37)$$

After that, the signal is mixed with the harmonic voltage of the RF generator driving the PM, with an additional phase ϕ . A mixer is basically a nonlinear electronic device that multiplies two signals. Multiplying V_{BP} by $\sin(\Omega_{\text{PDH}}t + \phi)$ leads to a DC component, which contains the information one is trying to extract, and to a $2\Omega_{\text{PDH}}$ component. At this point, one only has to use a low pass filter to retrieve the signal [29]. Recalling two trigonometric identities:

$$\cos(\Omega_{\text{PDH}}t) \cdot \sin(\Omega_{\text{PDH}}t + \phi) = \frac{1}{2}(\cos(2\Omega_{\text{PDH}}t + \phi) + \sin(\phi)) \quad (4.38)$$

$$\sin(\Omega_{\text{PDH}}t) \cdot \sin(\Omega_{\text{PDH}}t + \phi) = \frac{1}{2}(-\cos(2\Omega_{\text{PDH}}t + \phi) + \cos(\phi)) \quad (4.39)$$

One can see that multiplying V_{BP} by $\sin(\Omega_{\text{PDH}}t + \phi)$ and then low pass filtering yields to the following expression for V_{PDH} :

$$V_{\text{PDH}} \propto \text{Re}[\zeta(\omega)] \sin(\phi) + \text{Im}[\zeta(\omega)] \cos(\phi) \quad (4.40)$$

²As a reminder, the transfer function is the function such that $|R|^2 = \mathcal{R}$

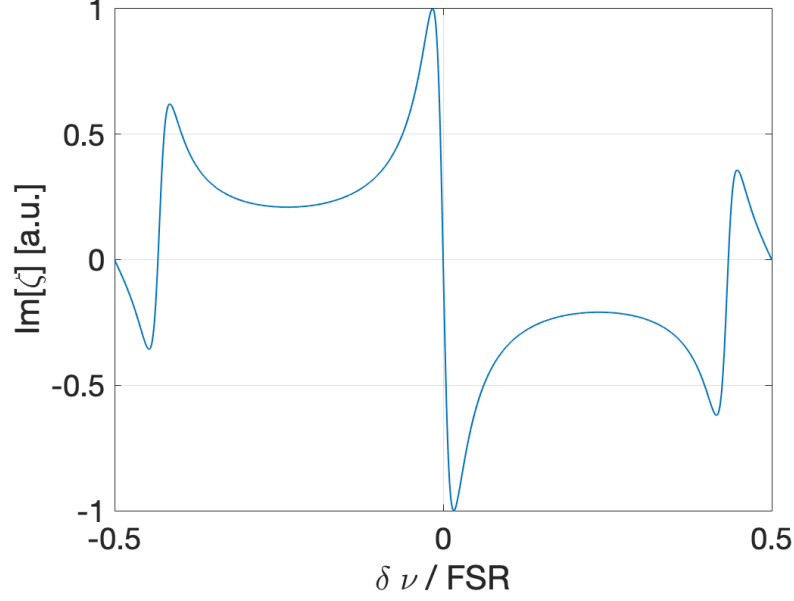


Figure 4.14: Normalised PDH error function ε as function of the normalised frequency $\delta\nu/\text{FSR}$ for a ring cavity with $\Omega_{\text{PDH}}/2\pi = 58\%$ of the FSR

One can therefore select which component to use by changing the value of ϕ . The PDH error function $\varepsilon(\omega)$ is defined as:

$$\varepsilon(\omega) = \text{Im}[\zeta(\omega)] \quad (4.41)$$

The graph of the PDH error function is depicted on figure 4.14. As required, it is antisymmetric with respect to the resonance frequency, which allows to immediately differentiate between an increase or a decrease of phase. Moreover, thanks to the steep slope of the curve at resonance, a small variation of phase implies a large variation of ε .

The end of the regulation scheme is the same as the previous one. The PDH signal V_{PDH} (with $\phi = 0$) is compared to a reference, which gives the error, and this error is used by the PID to regulate the laser. This scheme can stabilise the cavity at any phase, provided that the slope on the neighbourhood of this phase is steep enough. This condition is being quite vague, it should be checked experimentally whether it is possible to stabilise at a given phase.

4.4.3 Pound-Drever-Hall technique for the reservoir

The PDH technique can be applied to stabilise the reservoir. Yet, the error needs to be slightly modified to take into account the presence of different wavelengths inside the cavity. The result is actually quite straightforward if one recalls that the reflected field is simply given by $\mathbf{E}_{\text{ref}} = E_0 \sum_{n=-\eta}^{\eta} R_{n,0}(\omega) \hat{\mathbf{e}}_n$ thanks to the reservoir transfer matrix \mathbf{R} and that the PD cannot capture beatings whose frequencies are integer multiples of 20 GHz. With these two elements in mind, $\zeta(\omega)$ becomes:

$$\zeta(\omega) = \sum_{n=-\eta}^{\eta} R_{n,0}(\omega) R_{n,0}^*(\omega + \Omega_{\text{PDH}}) - R_{n,0}^*(\omega) R_{n,0}(\omega - \Omega_{\text{PDH}}) \quad (4.42)$$

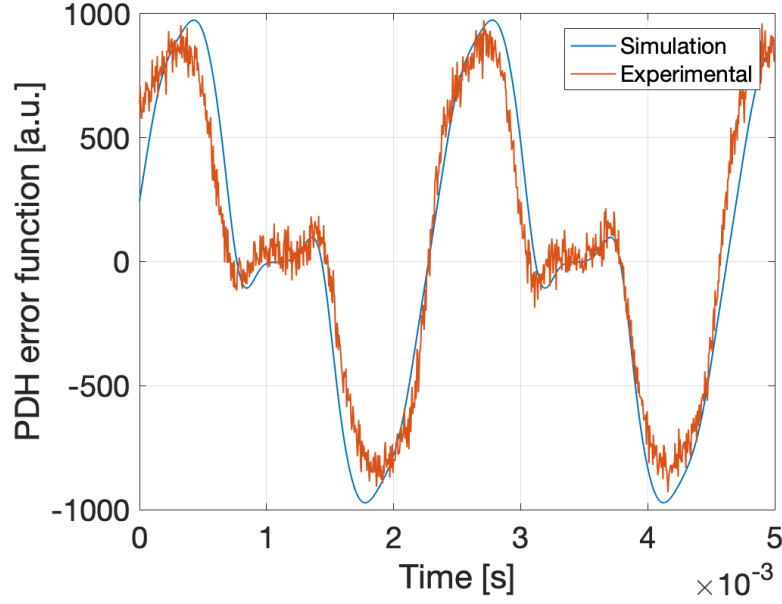


Figure 4.15: PDH error signal ε as a function of the time [s] for the reservoir cavity during a sweep of the Digilock. PDH Modulation amplitude $V_{\text{PDH}} = 0.4 V_{\text{PP}}$ (peak to peak), PDH modulation frequency $\nu_{\text{PDH}} = 3.13 \text{ MHz}$, intra-cavity modulation depth $m = 2$, intra-cavity modulation frequency $\nu_{\text{mod}} = 19.9998 \text{ GHz}$

The error function ε remains defined as the imaginary part of ζ . On figure 4.15, one can observe that the theoretical model is in line with the measured error function. The graph does not have the same shape as the one from figure 4.14, but since it exhibits regions with steep slopes, it can be used to stabilise the reservoir. In practice, the Digilock handles all the data-processing that has been introduced in this section, and the PID regulation as well.

4.5 Characterisation of the stabilisation performance for different regimes

This section presents the performances that can be achieved when stabilising the reservoir with the help of the PDH scheme, which is the core issue tackled in this thesis. First, the problem is recalled and specified in a comprehensive way, then the experimental procedure followed to obtain relevant data is presented, and finally the actual results are shown and discussed.

4.5.1 Introduction

The main issue that has prevented the reservoir from working so far is the complexity linked to the fact of keeping it stabilised for all the neurons at the same time. Given how efficient the PDH scheme is at stabilising cavities, it has been chosen to use it instead of the simple procedure relying only on the reflected power.

As already claimed, the PDH technique is capable of stabilising the cavity at any phase, provided that the slope of the PDH error function is steep enough for this phase. Therefore, one of the features being investigated experimentally is the determination of the

range of phases at which the cavity can be stabilised. This is of great practical importance, because as shown at section 3.9, the phase accumulated at each round trip is a global parameter that can alter the performances of the RC.

Another element that has been studied experimentally is the quality of the stabilisation. First, one has to use a relevant metric to assess how good the reservoir is stabilised. What is used throughout this section is the standard deviation of the phase during one run of measurements. Assume one is stabilising the reservoir at phase ϕ for some time. The phase inevitably fluctuates, but the better the cavity is stabilised, the lower these fluctuations. By recording the change of the phase, one can compute the standard deviation, the so-called phase noise, which therefore gives a quantitative indication on the efficiency of the stabilisation. This estimation can be done based on different kinds of signals, as it is explained in section 4.5.2.

The PDH technique also has its drawbacks. The phase modulation required to break the symmetry exhibited by the transfer function of the reservoir induces oscillations in the reflected power, whose amplitude is dependent on the experimental PDH parameters, namely the modulation amplitude and frequency. Intuitively, one can understand that if A_{PDH} and Ω_{PDH} are increased, this will result in larger oscillations. This is annoying because in general, boosting those parameters allows to obtain a sharper PDH error function, with a better SNR, ultimately enabling to reach a more robust stabilisation. A trade-off has to be found between a high-performance stabilisation scheme and low oscillation in the reflected power, as one does not want to improve one feature at the cost of completely deteriorating the other.

These different issues are investigated for different PDH phase modulation regimes, namely couple of values of A_{PDH} and Ω_{PDH} . At the end of the day, this thorough characterisation of the stabilisation properties of the reservoir allows one to choose the regulation parameters that lead to the best chance of making the RC work.

4.5.2 Approach

Before explaining the experimental procedure, a few points have to be discussed. First, compared to an actual RC experiment, the characterisation procedure is simplified because the amplitude of the electric field is not modulated by the MZM. In practice, the intensity modulation deteriorates the stabilisation signals, and this will need to be taken into account in the future, yet it has been neglected in the present analysis because not all challenges can be tackled at the same time. What is assumed, however, is that the PDH regime allowing to reach the best stabilisation is the same regardless of the intensity modulation being active or not.

To avoid any confusion, let us introduce the terminology used in this section:

- Transfer function: this is the transfer function of the cavity \mathcal{R} (time-independent)
- Reflected power: this is the power reflected by the reservoir (time-dependent)
- Error function: this is the PDH error function of the cavity ε (time-independent)
- Error signal: this is the instantaneous PDH error (time-dependent)

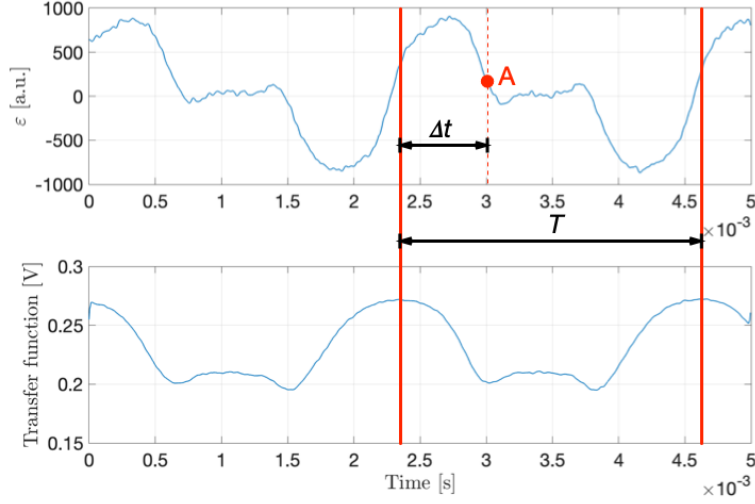


Figure 4.16: Error function [a.u.] and transfer function [V] as a function of the time [s] with $A_{\text{PDH}} = 0.4 V_{\text{PP}}$ and $\nu_{\text{PDH}} = 3.13 \text{ MHz}$, and schematic representation of the method followed to compute the phase.

As far as the experimental parameters are concerned, preliminary numerical simulations³ showed that the intra-cavity phase modulation frequency minimising the error rate of the reservoir when being used as a RC was $\nu_{\text{mod}} = 19.9998 \text{ GHz}$, with a modulation power $P_{\text{mod}} = 20 \text{ dBm}$ ($m = 2$). This modulation frequency is obtained by taking the one at which the first sideband is at resonance detuned by 500 kHz. It is therefore important to note that all the results of this section will only be valid for this modulation frequency, since changing it completely modifies the transfer and error functions of the reservoir. The characterisation covers different PDH regimes: the modulation frequency ν_{PDH} take the values 390 kHz, 781 kHz, 1.56 MHz and 3.13 MHz and the modulation amplitude V_{PDH} 0.2 V_{PP} , 0.3 V_{PP} and 0.4 V_{PP} . For all the frequencies, the three voltages are investigated except for $\nu_{\text{PDH}} = 390 \text{ kHz}$ where only $V_{\text{PDH}} = 0.4 V_{\text{PP}}$ is studied. A peculiarity of the regulation for the reservoir is that the proportional and derivative terms of the PID have no influence on the stabilisation. At this point, there is no clear explanation on why it is the case, but performing a proper characterisation of the step responses of all the devices involved in the regulation could bring some insight. Furthermore, the impact of the value of k_I , the integral coefficient on the PID, on the stabilisation is very limited. Several order of magnitude can be spanned without altering significantly the quality of the regulation. The coefficient was set heuristically to $k_I = 17\,000 \text{ V s}^{-1}$ because around this value the results seemed better, and was kept constant for all the measurements.

In the following paragraphs, the different quantities experimentally studied are presented, and the methodology followed to compute is explained.

Phase

The first key feature to determine is the phase at which one is stabilising. In practice, to choose the stabilisation position, a PDH error signal is selected as reference using the Digilock. To relate the PDH error signal value to an actual, one needs to use both the error signal and the transfer function, as depicted on figure 4.16. The transfer function is used to determine the position of the anti-resonance, located at the maxima, which

³Courtesy to Lorenz Butschek

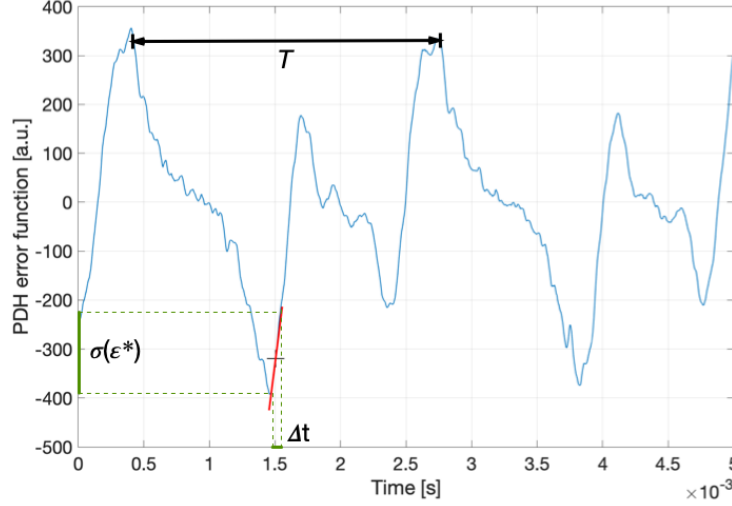


Figure 4.17: Error function as a function of the time [s] with $A_{\text{PDH}} = 0.4 V_{\text{PP}}$ and $\nu_{\text{PDH}} = 390 \text{ kHz}$, reservoir stabilised at $\varepsilon^* = -300 \text{ a.u.}$

corresponds to a phase of $\pm\pi \text{ rad}$. Let $A \equiv (t^*, \varepsilon^*)$ be the point whose y -coordinate corresponds to the reference error function value ε^* set up in the Digilock. If T is the delay between two maxima of the transfer function, and if Δt is the time interval between t^* and the first maximum, then the phase is given by:

$$\phi = -\pi + \frac{\Delta t}{T} 2\pi \quad (4.43)$$

Let the region of the PDH error function comprised between the two maxima of the transfer function be the restricted error function. For a given PDH error function value ε^* , if there exists several points $B \equiv (t, \varepsilon^*)$ in the restricted region, then it might be possible to stabilise at this value ε^* , but it will be impossible to infer the corresponding phase.

Pound-Drever-Hall signal

The next value of interest is the phase noise estimated based on the error signal. On the figure 4.18, one can see the evolution of the PDH error signal when the reservoir is being stabilised at -300 a.u. . Based on these data, one can easily compute the standard deviation of the error signal $\sigma(\varepsilon^*)$. This value still needs to be translated into a phase noise. To do so, one uses the error function displayed on the figure 4.17. First, one linearises the error function at the point of interest, which is represented by the red line segment on the figure. This allows to locally link $\sigma(\varepsilon^*)$ to a time variation Δt . The trick is to notice that the proportions are conserved between the phase space and the time space. In other words, the ratio between Δt and T (the delay between two maxima, as previously) is the same as the ratio between σ_{PDH} , the phase noise in rad, and 2π . If one defines α as the slope of the tangent at the point of interest (in a.u. s^{-1}), the phase noise reads:

$$\sigma_{\text{PDH}} = \frac{\sigma(\varepsilon^*)_{\text{PDH}}}{|\alpha|T} 2\pi \quad (4.44)$$

This justifies why it is better to work with steep slopes when using the PDH technique.

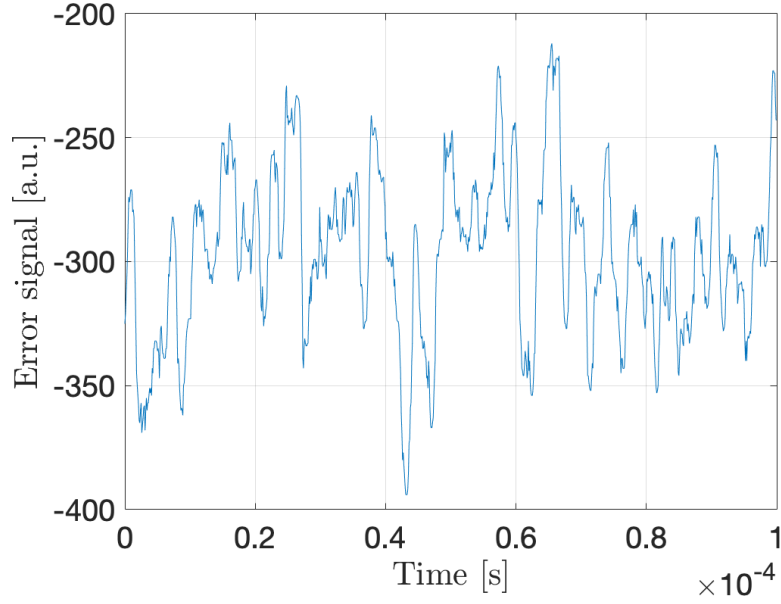


Figure 4.18: Error signal as a function of the time [s] with $A_{\text{PDH}} = 0.4 \text{ V}_{\text{PP}}$ and $\nu_{\text{PDH}} = 390 \text{ kHz}$, reservoir stabilised at $\varepsilon^* = -300 \text{ a.u.}$

Reflected power

The method to obtain the phase noise based on the reflected power is similar to that of the PDH error signal. The only difference is that it requires one more step, due to the fact that this time, the slope of the transfer function is needed instead of that of the error signal. On figures 4.19 and 4.21, one can see that, as mentioned in the introduction, the PDH phase modulation introduces oscillations. This implies that this transfer function cannot be used directly because linearising such an oscillating curve does not make much sense. Another solution has to be explored. The idea is to use a transfer function measured without PDH phase modulation, as the one displayed on figure 4.20. Let $A \equiv (\Delta t_1, \varepsilon^*)$ be the point at which the cavity is stabilised whose phase can be determined using the method presented above. Its x -coordinate can be reduced assuming that one is working in the restricted region. One would like to determine the point $B \equiv (\Delta t_2, V^*)$ on the figure 4.20 that has the same phase as A . If T denotes the delay between two maxima and if the indices 1,2 represent the transfer function and without phase modulation respectively, then Δt_2 simply reads:

$$\Delta t_2 = \frac{\Delta t_1}{T_1} T_2 \quad (4.45)$$

Once the coordinates of the point B are known, the principle is identical to that of the previous one: measure the slope α_2 of the transfer function at point B (in V s^{-1}), use the data from figure 4.21 to calculate the standard deviation $\sigma(\varepsilon^*)_{\text{ref}}$ (in V) and compute the phase noise σ_{ref} (in rad) as:

$$\sigma_{\text{ref}} = \frac{\sigma(\varepsilon^*)_{\text{ref}}}{|\alpha_2| T_2} 2\pi \quad (4.46)$$

Modulation intensity

The phase fluctuations in the reflected power have two components, the PDH phase modulation and the actual phase noise. In this paragraph, the method used to estimate

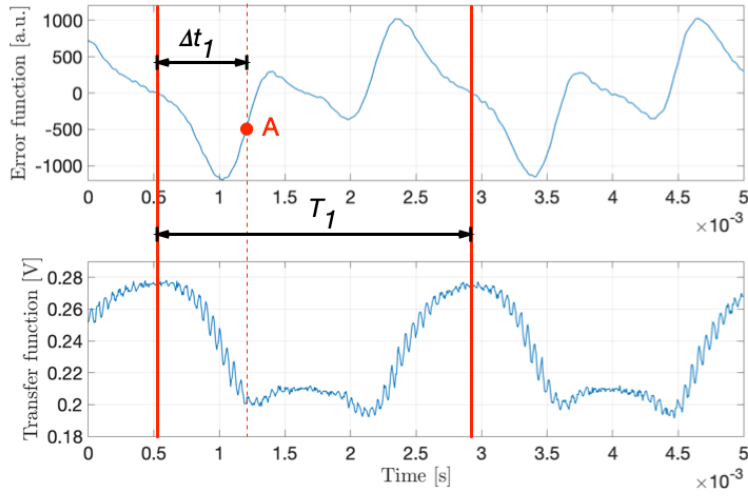


Figure 4.19: Error function and transfer function [V] as a function of the time [s], with $A_{\text{PDH}} = 0.4 \text{ V}_{\text{PP}}$ and $\nu_{\text{PDH}} = 781 \text{ kHz}$, and with the reservoir stabilised at $\varepsilon^* = -500 \text{ a.u.}$

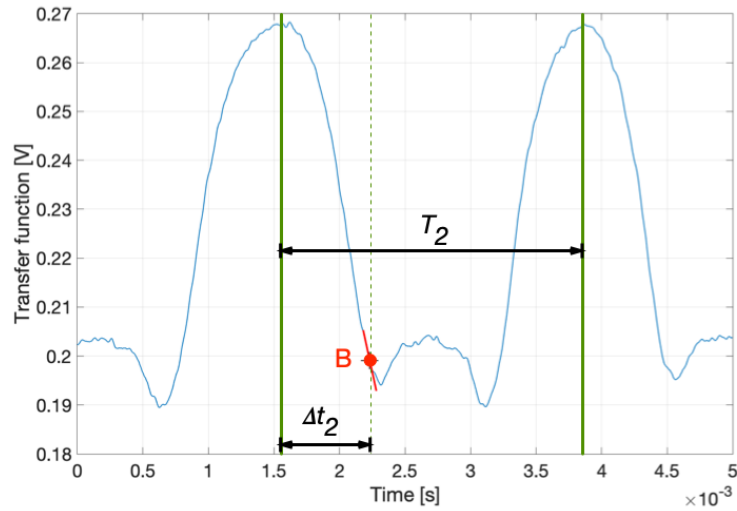


Figure 4.20: Transfer function [V] as a function of the time [s] without PDH modulation, with the reservoir stabilised at $\varepsilon^* = -500 \text{ a.u.}$

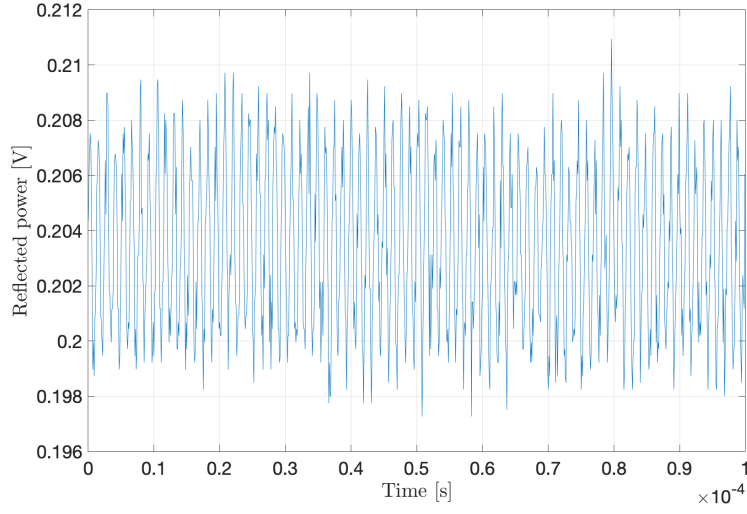


Figure 4.21: Reflected power [V] as a function of the time [s] with $A_{\text{PDH}} = 0.4 V_{\text{PP}}$ and $\nu_{\text{PDH}} = 781 \text{ kHz}$ and with the reservoir stabilised at $\varepsilon^* = -500 \text{ a.u.}$

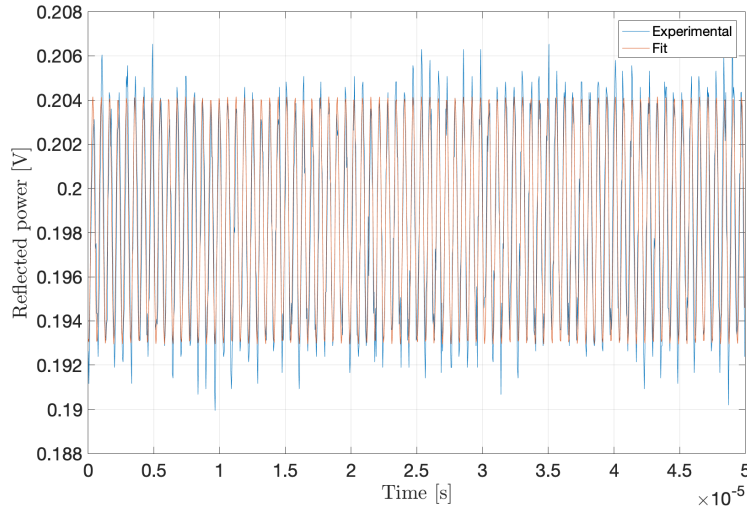


Figure 4.22: Reflected power [V] as a function of the time [s] with $A_{\text{PDH}} = 0.3 V_{\text{PP}}$ and $\nu_{\text{PDH}} = 1.56 \text{ MHz}$ and with the reservoir stabilised at $\varepsilon^* = 300 \text{ a.u.}$. Experimental data and sinusoidal fit.

the former is presented. The basic idea is to perform a least square fit, as presented in section 4.3.2, but this time using a sinusoidal function defined as:

$$\mathcal{V}_{\text{ref}}(t; \mathcal{A}, \theta, \mathcal{A}_0) = \mathcal{A} \sin(\Omega_{\text{PDH}} t + \theta) + \mathcal{A}_0 \quad (4.47)$$

With \mathcal{A} , φ and \mathcal{A}_0 being the three parameters to determine through the minimisation. Their value is given by:

$$(\mathcal{A}, \theta, \mathcal{A}_0) = \underset{(\mathcal{A}^*, \theta^*, \mathcal{A}_0^*)}{\text{argmin}} \sum_{i=0}^T (V_{\text{ref},i} - \mathcal{V}_{\text{ref}}(t_i; \mathcal{A}^*, \theta^*, \mathcal{A}_0^*))^2 \quad (4.48)$$

With T the total number of data points, $V_{\text{ref},i}$ the value of the reflected power and t_i the time of the i^{th} sample. On figure 4.22, the result of the optimisation is shown with the experimental data represented in blue, and the sinusoidal fitting in orange. It is now assumed that \mathcal{V}_{ref} is the part of the reflected power that is due to the phase modulation. The formula to compute the phase noise based on the transfer derived in the previous paragraph can be adapted to this situation by considering that the spreading of the signal is due to the oscillation amplitude \mathcal{A} (in V) rather than the standard deviation of the reflected power $\sigma(\varepsilon^*)_{\text{ref}}$. To avoid any confusion with respect to the PDH phase modulation, which comprises a modulation amplitude and frequency, this phase fluctuation is called to *modulation intensity*, $\Delta\varphi$ (in rad). It is given by:

$$\Delta\varphi = \frac{\mathcal{A}}{|\alpha_2|T_2} 2\pi \quad (4.49)$$

One is still working with reflected powers, therefore with transfer functions. Moreover, the stabilisation point, represented by B on the figure 4.20 has not changed, hence the use of the α_2 and T_2 in this new formula.

The apparition of this modulation intensity can be detrimental to the performances of the RC, but not in the same way as the phase noise. This can be understood by making the connection with the dynamics equation of the RC presented in equation (3.9). The phase noise has an influence on the phase matrix Φ by adding some fluctuations on the different phase factors, which can interpreted as an uncertainty on the phase acquired over one round trip. In contrast, the modulation intensity has an intrinsically different impact on the RC because it alters the input vector u . Indeed, instead of being simply expressed as $E_0 u(n) \exp(i\omega t)$, the input is compromised by a time-varying phase φ , which yields to $E_0 u(n) \exp(i(\omega t + \varphi))$ with $\varphi \in [0, \Delta\varphi]$. This implies that in the worst case scenario, the electric field entering the reservoir sees a change of phase of $\Delta\varphi$, whereas ideally the phase should have been kept constant, according to the definition of the input of a RC. Ironically, the modulation intensity that is observed because of the fact that the PDH technique is required to stabilise the reservoir could prevent it from working as a RC. This explains why both the phase noise and the modulation intensity need to be minimised.

Residual reflected power

What is called the residual reflected power is the part of the fluctuations of the reflected power that is not due to the oscillations. It is defined as:

$$V_{\text{res}}(t) = V_{\text{ref}}(t) - \mathcal{V}_{\text{ref}}(t) \quad (4.50)$$

The residual power coming from the signals depicted on the figure 4.22 is shown on figure 4.23. Once again, the previous formula can be used, provided that one uses $\sigma(\varepsilon^*)_{\text{res}}$

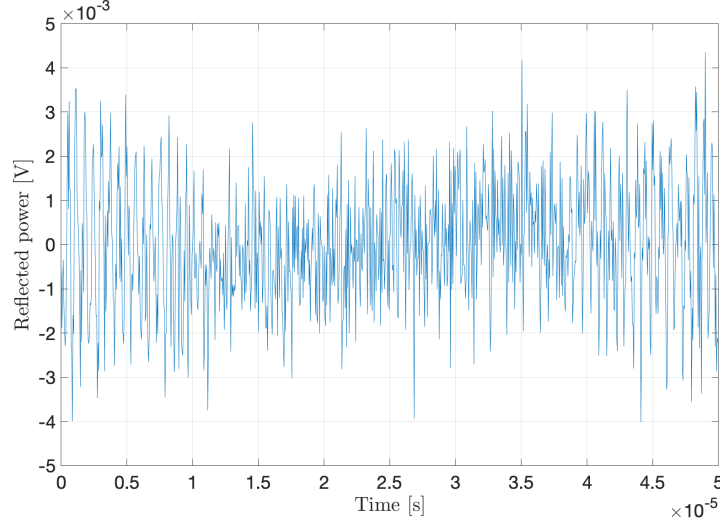


Figure 4.23: Residual reflected power [V] as a function of the time [s] with $A_{\text{PDH}} = 0.3 \text{ V}_{\text{PP}}$ and $\nu_{\text{PDH}} = 1.56 \text{ MHz}$ and with the reservoir stabilised at $\varepsilon^* = 300 \text{ a.u.}$

(in V) instead of $\sigma(\varepsilon^*)_{\text{ref}}$ to determine the phase noise based on the residual power σ_{res} (in rad):

$$\sigma_{\text{res}} = \frac{\sigma(\varepsilon^*)_{\text{res}}}{|\alpha_2|T_2} 2\pi \quad (4.51)$$

Long time-scale Pound-Drever-Hall signal

To be able to distinguish the modulation oscillations, the sampling frequency of the Digilock has to be at least twice the maximum PDH modulation frequency, which is 3.13 MHz, as required by the Shannon-Nyquist sampling theorem. To achieve higher sampling frequencies, the Digilock has to record data sets over shorter time-scales, as low as 50 μs , as can be seen on the time axis of the figure 4.23, for example. The problem is that the duration of a RC experiment is in the order of the ms. The long time-scale PDH phase noise is simply a generalisation of the PDH phase noise, but measured on a longer time-scale (5 ms), to ensure the robustness of the stabilisation scheme over the long run. Let $\sigma(\varepsilon^*)_{\text{PDH,l}}$ be the standard deviation of the PDH error signal recorded over 5 ms (in a.u.). The long time-scale PDH phase noise $\sigma_{\text{PDH,l}}$ (in rad) is computed in exactly the same way as the PDH phase noise, except that $\sigma(\varepsilon^*)_{\text{PDH,l}}$ is used instead of $\sigma(\varepsilon^*)_{\text{PDH}}$:

$$\sigma_{\text{PDH,l}} = \frac{\sigma(\varepsilon^*)_{\text{PDH,l}}}{|\alpha|T} 2\pi \quad (4.52)$$

4.5.3 Results

The results of the measurements can be found in the tables of the appendix A. For each PDH configuration and for each PDH stabilisation position ε^* , five data sets were measured in order to obtain results that are statistically more significant. In the tables, ϕ , σ_{PDH} , $\sigma_{\text{PDH,l}}$, σ_{ref} , $\Delta\varphi$ and σ_{res} are averages taken over the data sets, and $\mathcal{S}(\dots)$ are their respective standard deviations. The dimension of the different values is the mrad unless specified otherwise. For some ε^* , there is an additional value called the *challenger*. This is heuristic used to determine the best stabilisation configuration and position. It is defined as the product:

| Rank | A_{PDH} [V _{PP}] | ν_{PDH} [kHz] | ε^* [a.u.] | ϕ [rad] | Challenger [mrad ²] |
|------|-------------------------------------|--------------------------|------------------------|--------------|---------------------------------|
| #1 | 0.4 | 781 | 400 | 1.3 | 1166 |
| #2 | 0.2 | 781 | -300 | -1.43 | 1308 |
| #3 | 0.4 | 781 | 700 | 1.45 | 1349 |
| #4 | 0.3 | 781 | 500 | 1.31 | 1449 |
| #5 | 0.4 | 781 | 600 | 1.39 | 1506 |

Table 4.1: Top-5 ranking of the positions and configurations

$$\text{Challenger} = \sigma_{\text{PDH}} \cdot \Delta\varphi \quad (4.53)$$

Recalling that both σ_{PDH} and $\Delta\varphi$ should be as small as possible, the best configuration is the one minimising the challenger. Note that there might exist more sophisticated heuristics leading to better results, but the challenger was used as a first approach thanks to its simplicity. The challenger was only computed for stabilisation positions for which the confidence in the measurements is the highest, and that are supposed to be usable in a practical RC experiment. This condition excludes the positions:

- For which a given value of ε^* can correspond to different phases.
- At which the slope of the transfer function is close to zero, which means that one is close to a minimum. This implies that linearising the transfer function at this point is not very relevant because this approximation rapidly becomes invalid, and that the phase noises deduced from this operation can be inaccurate.
- Where σ_{PDH} , $\sigma_{\text{PDH,l}}$ and σ_{res} are not included in an interval 10 mrad wide, all at the same time. When they are included, it increases the confidence in the measurements because it suggests that similar phase noises can be obtained in three different ways.

Chapter 5

Conclusion

Appendix A

Experimental results

15

| ε^* [a.u.] | ϕ [rad] | σ_{PDH} | $\mathcal{S}(\sigma_{\text{PDH}})$ | $\sigma_{\text{PDH},1}$ | $\mathcal{S}(\sigma_{\text{PDH},1})$ | σ_{ref} | $\mathcal{S}(\sigma_{\text{ref}})$ | $\Delta\varphi$ | $\mathcal{S}(\Delta\varphi)$ | σ_{res} | $\mathcal{S}(\sigma_{\text{res}})$ | Challenger [mrad ²] |
|------------------------|--------------|-----------------------|------------------------------------|-------------------------|--------------------------------------|-----------------------|------------------------------------|-----------------|------------------------------|-----------------------|------------------------------------|---------------------------------|
| -300 | -1.61 | 44.08 | 4.56 | 44.78 | 1.11 | 72.05 | 3.55 | 86.93 | 3.09 | 37.5 | 3.37 | 3661 |
| -200 | -1.5 | 36.22 | 4.56 | 38.73 | 0.75 | 49.42 | 1.31 | 56.85 | 1.31 | 28.71 | 1.09 | 1964 |
| -100 | -1.4 | 22.53 | 3.68 | 22.97 | 0.81 | 59.07 | 1.69 | 56.89 | 1.94 | 43.23 | 1.2 | |
| -100 | 0.89 | 27.26 | 4.45 | 27.8 | 0.98 | 47.9 | 1.37 | 46.13 | 1.57 | 35.05 | 0.97 | |
| 100 | -1.22 | 56.69 | 12.72 | 57.4 | 1.86 | 85.39 | 4.09 | 81.11 | 3.74 | 63.18 | 4.35 | |
| 100 | 1.08 | 20.86 | 4.44 | 20.06 | 0.65 | 85.14 | 4.08 | 80.87 | 3.73 | 63 | 4.34 | |
| 200 | 1.18 | 35.49 | 4.88 | 38.56 | 1.46 | 88.79 | 2.1 | 102.11 | 2.2 | 51.59 | 2.42 | |
| -200 | -1.5 | | | 67.66 | 19.3 | 66.43 | 12.8 | | | | | |

Table A.1: Experimental results for PDH modulation amplitude $A_{\text{PDH}} = 0.4 \text{ V}_{\text{PP}}$, PDH modulation frequency $\nu_{\text{PDH}} = 390 \text{ kHz}$

| ε^* [a.u.] | ϕ [rad] | σ_{PDH} | $\mathcal{S}(\sigma_{\text{PDH}})$ | $\sigma_{\text{PDH,l}}$ | $\mathcal{S}(\sigma_{\text{PDH,l}})$ | σ_{ref} | $\mathcal{S}(\sigma_{\text{ref}})$ | $\Delta\varphi$ | $\mathcal{S}(\Delta\varphi)$ | σ_{res} | $\mathcal{S}(\sigma_{\text{res}})$ | Challenger [mrad ²] |
|------------------------|--------------|-----------------------|------------------------------------|-------------------------|--------------------------------------|-----------------------|------------------------------------|-----------------|------------------------------|-----------------------|------------------------------------|---------------------------------|
| -500 | -1.63 | 30.07 | 2.83 | 29.82 | 0.68 | 58.73 | 0.64 | 75.29 | 0.67 | 24.76 | 0.97 | 2124 |
| -400 | -1.53 | 50.21 | 4.58 | 51.12 | 0.75 | 53.83 | 0.71 | 66.02 | 1.45 | 26.71 | 1.37 | |
| -300 | -1.43 | 25.2 | 1.44 | 24.99 | 0.6 | 44.67 | 0.88 | 51.87 | 1.22 | 25.48 | 0.81 | |
| -200 | -1.36 | 23.8 | 1.4 | 23.37 | 0.38 | 139.88 | 2.73 | 143.53 | 6.36 | 96.11 | 2.94 | |
| -100 | -1.28 | 22.43 | 1.64 | 23.09 | 0.57 | 62.09 | 0.76 | 55.99 | 2.06 | 47.79 | 0.94 | |
| -100 | 0.83 | 42.68 | 3.12 | 43.94 | 1.09 | 39.38 | 0.48 | 35.51 | 1.31 | 30.31 | 0.6 | |
| 100 | -1.03 | 57.88 | 3.03 | 54.36 | 0.64 | 56.26 | 1.15 | 46.1 | 1.2 | 45.83 | 1.65 | 2354 |
| 100 | 1.06 | 22.15 | 1.16 | 20.81 | 0.24 | 123.14 | 2.51 | 100.89 | 2.63 | 100.31 | 3.62 | |
| 200 | 1.14 | 38.81 | 2.83 | 39.37 | 1.23 | 58.41 | 0.93 | 59.52 | 0.97 | 40.47 | 1.05 | |
| 300 | 1.22 | 22.82 | 1.51 | 23.44 | 0.57 | 79.75 | 2.13 | 93.18 | 2.81 | 44.88 | 1.07 | |
| 400 | 1.34 | 35.87 | 2.68 | 35.24 | 1.08 | 54.09 | 0.5 | 66.72 | 0.72 | 26.41 | 0.81 | 2169 |
| -300 | -1.43 | | | 46.75 | 13.1 | 69.36 | 17.87 | | | | | |

Table A.2: Experimental results for PDH modulation amplitude $A_{\text{PDH}} = 0.2 V_{\text{PP}}$, PDH modulation frequency $\nu_{\text{PDH}} = 781 \text{ kHz}$

| ε^* [a.u.] | ϕ [rad] | σ_{PDH} | $\mathcal{S}(\sigma_{\text{PDH}})$ | $\sigma_{\text{PDH,l}}$ | $\mathcal{S}(\sigma_{\text{PDH,l}})$ | σ_{ref} | $\mathcal{S}(\sigma_{\text{ref}})$ | $\Delta\varphi$ | $\mathcal{S}(\Delta\varphi)$ | σ_{res} | $\mathcal{S}(\sigma_{\text{res}})$ | Challenger [mrad ²] |
|------------------------|--------------|-----------------------|------------------------------------|-------------------------|--------------------------------------|-----------------------|------------------------------------|-----------------|------------------------------|-----------------------|------------------------------------|---------------------------------|
| -700 | -1.6 | 19.12 | 0.98 | 19.5 | 0.64 | 120.59 | 1.08 | 162.04 | 1.44 | 37.39 | 0.72 | |
| -600 | -1.55 | 17.16 | 0.73 | 17.55 | 0.34 | 82.78 | 1.07 | 109.33 | 1.21 | 29.48 | 1.03 | |
| -500 | -1.49 | 18.38 | 1.2 | 19.2 | 0.37 | 74.65 | 0.9 | 96.24 | 1.1 | 30.58 | 1.4 | |
| -400 | -1.45 | 16.56 | 1.07 | 16.25 | 0.34 | 58.53 | 1.06 | 73.56 | 1.4 | 26.77 | 0.63 | |
| -300 | -1.41 | 15.19 | 1.58 | 15.57 | 0.47 | 56.03 | 1.39 | 66.85 | 2.14 | 30.04 | 0.29 | |
| -200 | -1.37 | 15.06 | 1.44 | 14.3 | 0.32 | 151.58 | 3.48 | 167.17 | 3.88 | 94.82 | 2.49 | |
| -200 | 0.83 | 30.73 | 2.94 | 29.18 | 0.65 | 50.55 | 1.16 | 55.75 | 1.29 | 31.62 | 0.83 | |
| -100 | -1.32 | 14.29 | 1.23 | 14.37 | 0.18 | 82.11 | 1.4 | 83.89 | 2.25 | 56.73 | 1.36 | |
| -100 | 0.94 | 31.58 | 2.72 | 31.76 | 0.39 | 226.27 | 3.86 | 231.18 | 6.21 | 156.32 | 3.76 | |
| 100 | -1.17 | 23.69 | 1.79 | 24.66 | 0.36 | 87.12 | 1.58 | 88.71 | 2.3 | 60.42 | 0.77 | |
| 100 | 1.07 | 20.96 | 1.58 | 21.83 | 0.32 | 87.05 | 1.58 | 88.64 | 2.3 | 60.37 | 0.77 | |
| 200 | 1.14 | 19.99 | 1.72 | 20.4 | 0.56 | 63.5 | 0.77 | 69.63 | 1.31 | 40.07 | 0.78 | |
| 300 | 1.19 | 15.89 | 1.63 | 15.66 | 0.55 | 86.2 | 1.09 | 102.7 | 2.59 | 46.35 | 1.33 | |
| 400 | 1.24 | 21.7 | 2.62 | 21.98 | 0.62 | 79.12 | 0.67 | 99.28 | 1.31 | 36.41 | 1.33 | |
| 500 | 1.31 | 20.58 | 1.45 | 19.31 | 0.46 | 54.31 | 0.62 | 70.15 | 0.9 | 22.07 | 0.49 | 1449 |
| 600 | 1.35 | 19.2 | 1.21 | 19.59 | 0.57 | 76.25 | 0.65 | 100.99 | 1.13 | 26.91 | 0.8 | 2212 |
| -300 | -1.41 | | | 29.85 | 7.4 | 64.93 | 7.02 | | | | | |

Table A.3: Experimental results for PDH modulation amplitude $A_{\text{PDH}} = 0.3 \text{ V}_{\text{PP}}$, PDH modulation frequency $\nu_{\text{PDH}} = 781 \text{ kHz}$

| ε^* [a.u.] | ϕ [rad] | σ_{PDH} | $\mathcal{S}(\sigma_{\text{PDH}})$ | $\sigma_{\text{PDH,l}}$ | $\mathcal{S}(\sigma_{\text{PDH,l}})$ | σ_{ref} | $\mathcal{S}(\sigma_{\text{ref}})$ | $\Delta\varphi$ | $\mathcal{S}(\Delta\varphi)$ | σ_{res} | $\mathcal{S}(\sigma_{\text{res}})$ | Challenger [mrad ²] |
|------------------------|--------------|-----------------------|------------------------------------|-------------------------|--------------------------------------|-----------------------|------------------------------------|-----------------|------------------------------|-----------------------|------------------------------------|---------------------------------|
| -1000 | -1.7 | 27.64 | 1.15 | 30 | 0.39 | 86.27 | 0.89 | 118.52 | 1.26 | 20.26 | 1.41 | 3078 |
| -900 | -1.63 | 18.19 | 1.43 | 18.06 | 0.38 | 99.96 | 0.63 | 136.75 | 0.85 | 25.15 | 1.12 | 2799 |
| -800 | -1.59 | 13.68 | 1.51 | 14.26 | 0.23 | 148.32 | 1.62 | 201.66 | 1.63 | 40.53 | 2.26 | |
| -700 | -1.55 | 17.9 | 1.57 | 17.39 | 0.47 | 95.42 | 0.76 | 128.27 | 1.45 | 29.51 | 1.41 | 2771 |
| -600 | -1.49 | 22.7 | 1.51 | 23.68 | 0.45 | 88.02 | 0.26 | 117.12 | 0.51 | 29.65 | 1.25 | 2968 |
| -500 | -1.44 | 15.5 | 2.67 | 15.97 | 0.52 | 68.54 | 0.93 | 89.22 | 1.62 | 26.7 | 1.56 | |
| -400 | -1.39 | 14.74 | 1.99 | 13.94 | 0.2 | 96.58 | 0.96 | 122.41 | 2.06 | 42.73 | 1.32 | |
| -300 | -1.37 | 13.69 | 1.58 | 14.39 | 0.36 | 193.24 | 4.22 | 234.45 | 5.83 | 99.04 | 3.73 | |
| -200 | -1.31 | 16.4 | 0.58 | 18.1 | 0.49 | 81.43 | 1.06 | 94.16 | 0.84 | 46.81 | 1.32 | |
| -200 | 0.98 | 20.92 | 0.73 | 23.09 | 0.62 | 811.36 | 10.55 | 938.23 | 8.38 | 466.49 | 13.14 | |
| -100 | -1.27 | 16.11 | 1.8 | 16.96 | 0.32 | 75.19 | 1.42 | 82.55 | 2.25 | 47.37 | 0.75 | |
| -100 | 1.03 | 23.41 | 2.61 | 24.64 | 0.47 | 295.7 | 5.58 | 324.64 | 8.84 | 186.3 | 2.96 | |
| 100 | -1.16 | 17.58 | 1.35 | 18.33 | 0.35 | 74 | 1.61 | 83.13 | 2.44 | 44.9 | 0.95 | |
| 100 | 1.16 | 17.06 | 1.31 | 17.79 | 0.34 | 64.79 | 1.41 | 72.79 | 2.13 | 39.31 | 0.83 | |
| 200 | 1.21 | 18.21 | 2.24 | 16.89 | 0.36 | 76.27 | 1.34 | 87.42 | 2.29 | 44.62 | 1.41 | |
| 300 | 1.26 | 15.76 | 1.37 | 15.17 | 0.37 | 63.15 | 0.93 | 75.55 | 1.93 | 33.59 | 1.03 | |
| 400 | 1.3 | 15.25 | 1.46 | 16.94 | 0.43 | 50.43 | 1.24 | 63.56 | 1.7 | 22.83 | 0.82 | 1166 |
| 500 | 1.34 | 20.11 | 1.62 | 19.45 | 0.49 | 65.75 | 0.8 | 85.45 | 1.37 | 25.84 | 0.82 | 1863 |
| 600 | 1.39 | 19.43 | 1.51 | 19.06 | 0.25 | 58.27 | 0.5 | 77.42 | 0.63 | 19.87 | 0.49 | 1506 |
| 700 | 1.45 | 17.96 | 0.89 | 19.75 | 0.35 | 55.31 | 0.32 | 74.6 | 0.52 | 16.55 | 0.66 | 1349 |
| 800 | 1.5 | 21.76 | 1.64 | 22.96 | 0.95 | 58.1 | 0.36 | 78.98 | 0.35 | 15.88 | 0.52 | 1595 |
| -400 | -1.39 | | | 37.98 | 9.55 | 110.43 | 6.02 | | | | | |

Table A.4: Experimental results for PDH modulation amplitude $A_{\text{PDH}} = 0.4 V_{\text{PP}}$, PDH modulation frequency $\nu_{\text{PDH}} = 781 \text{ kHz}$

| ε^* [a.u.] | ϕ [rad] | σ_{PDH} | $\mathcal{S}(\sigma_{\text{PDH}})$ | $\sigma_{\text{PDH,l}}$ | $\mathcal{S}(\sigma_{\text{PDH,l}})$ | σ_{ref} | $\mathcal{S}(\sigma_{\text{ref}})$ | $\Delta\varphi$ | $\mathcal{S}(\Delta\varphi)$ | σ_{res} | $\mathcal{S}(\sigma_{\text{res}})$ | Challenger [mrad ²] |
|------------------------|--------------|-----------------------|------------------------------------|-------------------------|--------------------------------------|-----------------------|------------------------------------|-----------------|------------------------------|-----------------------|------------------------------------|---------------------------------|
| -400 | -1.92 | 82.81 | 2.17 | 83.66 | 1.65 | 61.38 | 0.86 | 81.48 | 1.18 | 21.08 | 0.63 | 2398 |
| -300 | -1.68 | 75.12 | 2.51 | 75.5 | 0.6 | 54.5 | 1.01 | 71.26 | 1.39 | 20.7 | 0.44 | |
| -200 | -1.56 | 31.03 | 1.21 | 31.78 | 0.59 | 62.77 | 1.41 | 80 | 2.35 | 27.13 | 0.29 | |
| -100 | -1.42 | 28.89 | 2.13 | 39.18 | 0.71 | 43.93 | 1.06 | 53.47 | 1.19 | 22.32 | 0.89 | |
| 100 | 0.83 | 58.03 | 5.66 | 56.7 | 1.52 | 51.63 | 0.9 | 62.55 | 1.48 | 26.58 | 0.52 | |
| 200 | 0.93 | 38.04 | 0.65 | 37.88 | 0.3 | 341.89 | 7.41 | 431.8 | 9 | 153.51 | 4.75 | |
| 300 | 1.05 | 66.03 | 5.52 | 63.4 | 0.97 | 281.99 | 4.72 | 369.3 | 6.85 | 106.09 | 1.31 | |
| -200 | -1.56 | | | 36.91 | 3 | 72.95 | 4.75 | | | | | |

Table A.5: Experimental results for PDH modulation amplitude $A_{\text{PDH}} = 0.2 V_{\text{PP}}$, PDH modulation frequency $\nu_{\text{PDH}} = 1.56 \text{ MHz}$

| ε^* [a.u.] | ϕ [rad] | σ_{PDH} | $\mathcal{S}(\sigma_{\text{PDH}})$ | $\sigma_{\text{PDH,l}}$ | $\mathcal{S}(\sigma_{\text{PDH,l}})$ | σ_{ref} | $\mathcal{S}(\sigma_{\text{ref}})$ | $\Delta\varphi$ | $\mathcal{S}(\Delta\varphi)$ | σ_{res} | $\mathcal{S}(\sigma_{\text{res}})$ | Challenger [mrad ²] |
|------------------------|--------------|-----------------------|------------------------------------|-------------------------|--------------------------------------|-----------------------|------------------------------------|-----------------|------------------------------|-----------------------|------------------------------------|---------------------------------|
| -500 | -1.6 | 40.98 | 2.35 | 40.95 | 0.77 | 176.42 | 3.46 | 237.8 | 4.54 | 53.1 | 2.49 | 6936 |
| -400 | -1.45 | 45.42 | 3.83 | 47.46 | 1.35 | 118.11 | 2.35 | 158.27 | 3.32 | 37.59 | 0.74 | |
| -300 | -1.37 | 29.93 | 2.45 | 28.63 | 0.71 | 366.37 | 4.22 | 485.97 | 6.13 | 126.58 | 1.63 | |
| -200 | -1.3 | 46.57 | 3.07 | 45.99 | 1.08 | 158.49 | 1.79 | 206.94 | 2.45 | 60.7 | 1.14 | |
| -100 | -1.2 | 78.61 | 8.94 | 79.71 | 1.33 | 1486.13 | 9.35 | 1905.17 | 21.69 | 625.83 | 11.57 | |
| 100 | -0.98 | 86.12 | 3.33 | 83.91 | 3.26 | 107.14 | 1.67 | 136.49 | 2.79 | 46.41 | 0.67 | |
| 100 | 1.04 | 49.25 | 1.9 | 47.98 | 1.86 | 2076.51 | 32.34 | 2645.29 | 54.07 | 899.52 | 13.01 | |
| 200 | 1.15 | 38.2 | 3.1 | 38.51 | 0.85 | 128.41 | 2.87 | 167.41 | 4.09 | 49.61 | 0.83 | 10857 |
| 300 | 1.23 | 55.16 | 2.82 | 56.14 | 1.47 | 149.91 | 0.87 | 198.17 | 2.05 | 53.06 | 1.76 | |
| 400 | 1.37 | 36.98 | 1.66 | 37.08 | 1.01 | 101.77 | 0.95 | 136.52 | 1.23 | 32.07 | 0.62 | 4830 |
| 500 | 1.45 | 163.53 | 12.6 | 177.98 | 2.9 | 82.01 | 1.34 | 110.51 | 1.97 | 24.76 | 0.66 | |
| -300 | -1.37 | | | 38.9 | 3.71 | 388.43 | 7.61 | | | | | |

Table A.6: Experimental results for PDH modulation amplitude $A_{\text{PDH}} = 0.3 V_{\text{PP}}$, PDH modulation frequency $\nu_{\text{PDH}} = 1.56 \text{ MHz}$

| ε^* [a.u.] | ϕ [rad] | σ_{PDH} | $\mathcal{S}(\sigma_{\text{PDH}})$ | $\sigma_{\text{PDH,l}}$ | $\mathcal{S}(\sigma_{\text{PDH,l}})$ | σ_{ref} | $\mathcal{S}(\sigma_{\text{ref}})$ | $\Delta\varphi$ | $\mathcal{S}(\Delta\varphi)$ | σ_{res} | $\mathcal{S}(\sigma_{\text{res}})$ | Challenger [mrad ²] |
|------------------------|--------------|-----------------------|------------------------------------|-------------------------|--------------------------------------|-----------------------|------------------------------------|-----------------|------------------------------|-----------------------|------------------------------------|---------------------------------|
| -800 | -1.74 | 56.81 | 3.38 | 57.23 | 1.27 | 146.55 | 0.69 | 199.55 | 0.96 | 39.3 | 0.93 | 13518 |
| -700 | -1.61 | 46.18 | 2.82 | 46.64 | 0.6 | 202.34 | 1.29 | 275.47 | 2.01 | 54.4 | 1.08 | |
| -600 | -1.54 | 25.99 | 1.69 | 25.21 | 0.42 | 171.36 | 2.28 | 232.4 | 2.79 | 48.26 | 1.69 | |
| -500 | -1.47 | 48.03 | 2.19 | 47.11 | 0.5 | 149.37 | 1.95 | 201.31 | 2.54 | 44.12 | 1.1 | 9363 |
| -400 | -1.33 | 24.95 | 1.5 | 24.65 | 0.79 | 480.5 | 3.53 | 644.16 | 4.61 | 152.3 | 2.89 | |
| -300 | -1.35 | 39.26 | 3.71 | 39.63 | 0.47 | 535.94 | 7.95 | 713.98 | 13.87 | 178.9 | 8.88 | |
| -200 | -1.28 | 24.3 | 1.8 | 24.02 | 0.4 | 188.77 | 2.24 | 249.37 | 3.22 | 67.14 | 1.41 | |
| -100 | -1.21 | 79.43 | 3.88 | 78.96 | 2.52 | 359.78 | 2.99 | 473.63 | 3.18 | 130.94 | 5.62 | |
| -100 | 0.7 | 33.14 | 1.62 | 32.95 | 1.05 | 103.46 | 0.86 | 136.2 | 0.92 | 37.65 | 1.62 | |
| 100 | -1.04 | 62.38 | 6.29 | 62.1 | 2.17 | 192.32 | 1.46 | 251.94 | 2.02 | 72.25 | 1.21 | |
| 100 | 0.84 | 88.35 | 8.91 | 87.96 | 3.08 | 93.53 | 0.71 | 122.51 | 0.98 | 35.14 | 0.59 | |
| 200 | 0.95 | 37.52 | 2 | 41.91 | 1.35 | 3063.85 | 16.68 | 4048.26 | 18.91 | 1088.31 | 22.56 | |
| 300 | 1.02 | 23.5 | 1.96 | 23.25 | 0.53 | 407.62 | 4.32 | 542.7 | 7.18 | 136.82 | 4.82 | |
| 400 | 1.07 | 68.29 | 2.78 | 67.91 | 1.29 | 313.75 | 5.02 | 422.95 | 6.9 | 94.36 | 2.63 | |
| 500 | 1.16 | 41.94 | 0.9 | 40.04 | 0.54 | 256.52 | 1.32 | 347.05 | 1.49 | 74.3 | 1.39 | |
| 600 | 1.25 | 33.25 | 1.88 | 34.64 | 0.43 | 207.43 | 2.25 | 281.17 | 3.01 | 58.77 | 1.88 | 11549 |
| 700 | 1.36 | 53.34 | 6.04 | 56.33 | 1.63 | 165.25 | 0.96 | 225.04 | 1.32 | 44.29 | 0.4 | |
| -400 | -1.33 | | | 37.95 | 5.01 | 503.69 | 12.07 | | | | | |

Table A.7: Experimental results for PDH modulation amplitude $A_{\text{PDH}} = 0.4 V_{\text{PP}}$, PDH modulation frequency $\nu_{\text{PDH}} = 1.56 \text{ MHz}$

| ε^* [a.u.] | ϕ [rad] | σ_{PDH} | $\mathcal{S}(\sigma_{\text{PDH}})$ | $\sigma_{\text{PDH,l}}$ | $\mathcal{S}(\sigma_{\text{PDH,l}})$ | σ_{ref} | $\mathcal{S}(\sigma_{\text{ref}})$ | $\Delta\varphi$ | $\mathcal{S}(\Delta\varphi)$ | σ_{res} | $\mathcal{S}(\sigma_{\text{res}})$ | Challenger [mrad ²] |
|------------------------|--------------|-----------------------|------------------------------------|-------------------------|--------------------------------------|-----------------------|------------------------------------|-----------------|------------------------------|-----------------------|------------------------------------|---------------------------------|
| -300 | 1.36 | 43.53 | 2.89 | 44.22 | 1.31 | 127.61 | 0.73 | 174.38 | 1.21 | 32.53 | 0.54 | 6548 |
| -200 | 1.17 | 43.35 | 1.79 | 43.66 | 0.83 | 213.93 | 3.03 | 290.42 | 4.02 | 59.64 | 1.36 | |
| -100 | 0.99 | 63.78 | 5.45 | 67.44 | 1.83 | 506.7 | 5.39 | 684.67 | 6.98 | 148.97 | 2.58 | |
| 100 | -1.37 | 26.37 | 2.21 | 26.91 | 0.5 | 249.57 | 0.74 | 337.93 | 1.16 | 71.44 | 1.88 | |
| 200 | -1.51 | 46.06 | 3.27 | 49.39 | 1.14 | 128.44 | 1.31 | 174.74 | 1.37 | 23.75 | 1.28 | |
| 300 | -1.63 | 40.8 | 2.03 | 41.51 | 0.7 | 125.19 | 1.33 | 170.8 | 1.6 | 32.71 | 1.71 | |
| -200 | 1.17 | | | 50.14 | 5.75 | 232.03 | 14.0 | | | | | |

Table A.8: Experimental results for PDH modulation amplitude $A_{\text{PDH}} = 0.2 V_{\text{PP}}$, PDH modulation frequency $\nu_{\text{PDH}} = 3.13 \text{ MHz}$

| ε^* [a.u.] | ϕ [rad] | σ_{PDH} | $\mathcal{S}(\sigma_{\text{PDH}})$ | $\sigma_{\text{PDH,l}}$ | $\mathcal{S}(\sigma_{\text{PDH,l}})$ | σ_{ref} | $\mathcal{S}(\sigma_{\text{ref}})$ | $\Delta\varphi$ | $\mathcal{S}(\Delta\varphi)$ | σ_{res} | $\mathcal{S}(\sigma_{\text{res}})$ | Challenger [mrad ²] |
|------------------------|--------------|-----------------------|------------------------------------|-------------------------|--------------------------------------|-----------------------|------------------------------------|-----------------|------------------------------|-----------------------|------------------------------------|---------------------------------|
| -400 | 1.09 | 50.9 | 2.5 | 50.18 | 1.03 | 457.92 | 5.51 | 631.29 | 7.34 | 102.51 | 3.85 | 8641 |
| -300 | 0.99 | 34.07 | 3.02 | 36.1 | 0.66 | 872.16 | 7.82 | 1200.15 | 11.8 | 199.09 | 1.82 | |
| -200 | 0.92 | 29.03 | 1.78 | 29.26 | 0.58 | 434.95 | 2.36 | 597.01 | 2.44 | 103.86 | 2.48 | |
| -100 | 0.79 | 34.45 | 2.27 | 35.84 | 0.76 | 201.78 | 1.67 | 276.41 | 2.45 | 49.74 | 0.54 | |
| 100 | -1.43 | 43.45 | 2.92 | 43.92 | 1.24 | 151.95 | 1.18 | 208.24 | 1.46 | 37.12 | 0.86 | |
| 200 | -1.5 | 21.58 | 1.65 | 22.11 | 0.54 | 172.69 | 1.23 | 237.59 | 1.75 | 39.71 | 1.29 | |
| 300 | -1.58 | 82.67 | 5.89 | 82.63 | 1.26 | 238.24 | 2.1 | 237.66 | 2.82 | 55.05 | 1.07 | 5422 |
| 400 | -1.67 | 27.8 | 1.94 | 29.58 | 0.33 | 134.92 | 1.85 | 185.91 | 2.69 | 30.12 | 0.36 | |
| 500 | -1.76 | 51.79 | 5.36 | 54.13 | 1.55 | 166.61 | 0.81 | 229.92 | 1.3 | 36.21 | 0.79 | |
| -200 | 0.92 | | | 41.04 | 6.77 | 449 | 13.55 | | | | | |

Table A.9: Experimental results for PDH modulation amplitude $A_{\text{PDH}} = 0.3 V_{\text{PP}}$, PDH modulation frequency $\nu_{\text{PDH}} = 3.13 \text{ MHz}$

| ε^* [a.u.] | ϕ [rad] | σ_{PDH} | $\mathcal{S}(\sigma_{\text{PDH}})$ | $\sigma_{\text{PDH,l}}$ | $\mathcal{S}(\sigma_{\text{PDH,l}})$ | σ_{ref} | $\mathcal{S}(\sigma_{\text{ref}})$ | $\Delta\varphi$ | $\mathcal{S}(\Delta\varphi)$ | σ_{res} | $\mathcal{S}(\sigma_{\text{res}})$ | Challenger [mrad ²] |
|------------------------|--------------|-----------------------|------------------------------------|-------------------------|--------------------------------------|-----------------------|------------------------------------|-----------------|------------------------------|-----------------------|------------------------------------|---------------------------------|
| -600 | 1.23 | 48.12 | 2.35 | 51.04 | 0.87 | 449.73 | 18.23 | 622.56 | 25.44 | 90.98 | 2.72 | |
| -500 | 1.13 | 42.15 | 5.84 | 44.19 | 0.83 | 413.87 | 4.17 | 572.72 | 6.23 | 85.52 | 1.41 | |
| -400 | 1.04 | 33.34 | 2.12 | 33.68 | 1.05 | 8003.43 | 1060.52 | 11069.88 | 1477.35 | 1654.19 | 166.46 | |
| -300 | 0.98 | 29.17 | 2.91 | 30.8 | 0.5 | 1058.93 | 4.87 | 1460.57 | 8.41 | 232.23 | 7.18 | |
| -200 | 0.89 | 43.98 | 4.85 | 43.71 | 0.94 | 269.26 | 0.97 | 371.15 | 1.56 | 59.97 | 1.88 | |
| -100 | 0.84 | 23.73 | 1.52 | 24.47 | 0.56 | 229.04 | 2.42 | 315.13 | 3.32 | 52.53 | 1.54 | |
| 100 | -1.29 | 45.6 | 3.03 | 46.78 | 1.15 | 324.74 | 1.87 | 444.04 | 3.53 | 82.11 | 1.82 | |
| 200 | -1.38 | 37.63 | 2.52 | 38.08 | 0.36 | 480.09 | 3.17 | 662.14 | 4.18 | 105.44 | 2.87 | |
| 300 | -1.44 | 27.54 | 1.44 | 28.7 | 0.69 | 230.14 | 2.24 | 317.6 | 3.25 | 49.77 | 0.89 | |
| 400 | -1.5 | 25.84 | 2.88 | 26.88 | 0.89 | 263.58 | 1.45 | 364.3 | 2.04 | 55 | 1.63 | |
| 500 | -1.56 | 33.57 | 1.96 | 33.52 | 0.6 | 299.22 | 1.78 | 413.79 | 2.43 | 62.41 | 0.96 | |
| 600 | -1.64 | 29.88 | 2.27 | 30.64 | 0.61 | 216 | 0.73 | 298.92 | 1.07 | 44.01 | 0.69 | |
| 700 | -1.7 | 32.09 | 3.42 | 32.58 | 0.28 | 206.02 | 0.95 | 285.37 | 1.49 | 41.28 | 0.39 | 10078 |
| -300 | 0.98 | | | 45.28 | 7.62 | 1072.04 | 11.6 | | | | | |

Table A.10: Experimental results for PDH modulation amplitude $A_{\text{PDH}} = 0.4 V_{\text{PP}}$, PDH modulation frequency $\nu_{\text{PDH}} = 3.13 \text{ MHz}$

Appendix B

Specifications

Laser NKT Photonics: Koheras Basik Module Fiber laser, Model: K82-152-13, SNR: 60 dB, Wavelength: 1550.12 nm, Linewidth: <100 Hz, Maximum output power: 200 mW, Piezo tuning: 0.1 pm/V @ 100 Hz [22]

Mach-Zehnder Modulator iXblue MX-LN-10, Bandwidth: 12 GHz, $V_{\pi,RF}$ @ 50 kHz: 5.5 V, $V_{\pi,DC}$: 6.5 V, Extinction ratio: 22 dB, Insertion loss: 3.5 dB [28]

Intra-cavity Phase Modulator EOspace Ultra-Low V_{π} phase modulator, 3 dB Bandwidth: 25 GHz, $V_{\pi,RF}$ @ 1 GHz: 2.7 V, Optical return loss: 50 dB, Insertion loss: 4 dB [1]

Arbitrary Wave Generator NI PXI-5422, 16 bits 200 MSamples/s, Bandwidth: 80 MHz [34]

Photodiodes TTI TIA-525, Bandwidth: 120 MHz [39]

Digitizer NI PXI-5124, 12 bits, 200 MSamples/s, Bandwidth: 150 MHz [33]

Band pass filter Finisar WaveShaper 4000S, Operating frequency range: 191.250 THz to 196.275 THz (1527.4 nm to 1567.5 nm), Insertion loss: 4.5 to 6.5 dB, Filter Bandwidth: 10 GHz-5 THz [45]

Boost Optical Amplifier Thorlabs BOA 1004P SOA, Wavelength range: 1530-1570 nm, Output power: 15 dBm, Gain: 27 dB [8]

Intra-cavity Erbium-Doped Fibre Amplifier Keopsys CEFA-C-BO-HP-PM, Wavelength range: 1540-1565 nm, Output power: 27 dBm, Input power range: 5-15 dBm [9]

Digilock Toptica Digilock 110, PDH frequencies: 1.56 to 25 MHz, Lock-In Amplification frequencies: 12 Hz to 781 kHz [11]

PDH Phase Modulator iXblue MPZ-LN-10-00-PP-FAFA, 3 dB Bandwidth: 16.3 GHz, $V_{\pi,RF}$ @ 50 kHz: 6.75 V, Optical return loss: 45 dB, Insertion loss: 3 dB [27]

Pre-amp Erbium-Doped Fibre Amplifier Pritel PMFA-15, Wavelength range: 1530-1565 nm, Output power: 15 dBm, Input power range: -30 to 10 dBm [32]

Acronyms

| | |
|--------------|---|
| AWG | Arbitrary Wave Generator 26, 59 |
| EDFA | Erbium-Doped Fibre Amplifier 27, 28, 33, 59 |
| ESN | Echo State Network 7, 8, 14 |
| FP | Fabry-Perot 22–24, 28, 33 |
| FSR | Free Spectral Range 18, 22, 23, 25, 31, 33, 39 |
| ML | Machine Learning 7, 8, 10 |
| MZM | Mach-Zehnder Modulator 13, 18, 26, 27, 41, 59 |
| NARMA | Nonlinear Auto-Regressive Moving Average 15 |
| NMSE | Normalised Mean Square Error 11, 15, 19 |
| NN | Neural Network 7, 8, 12, 14 |
| PD | Photodiode 18, 30, 31, 36, 38, 39, 59 |
| PDH | Pound-Drever-Hall 27, 35–45, 47, 48, 51–59 |
| PID | Proportional-Integral-Derivative 25, 36, 37, 39, 40, 42 |
| PM | Phase Modulator 17–21, 25–29, 33, 36, 38, 59 |
| PRC | Photonic Reservoir Computing 11–13, 17, 18, 26 |
| RC | Reservoir Computer 7–12, 14, 16–20, 41, 42, 47, 48 |
| RC | Reservoir Computing 7, 10, 13, 14, 49 |
| RNN | Recurrent Neural Network 7 |
| RTT | Round Trip Time 12, 18 |
| SER | Signal Error Rate 16 |
| SNR | Signal to Noise Ratio 16, 27, 41 |
| SOA | Semiconductor Optical Amplifier 11, 13, 27, 59 |
| TDM | Time Division Multiplexing 7, 11–13, 17 |
| WDM | Wavelength Division Multiplexing 17, 18, 26 |

Bibliography

- [1] A. Akrout et al. “Parallel photonic reservoir computing using frequency multiplexing of neurons”. In: (2016).
- [2] Piotr Antonik et al. “Online Training of an Opto-Electronic Reservoir Computer Applied to Real-Time Channel Equalization”. In: *IEEE Transactions on Neural Networks and Learning Systems* 28.11 (Nov. 2017), pp. 2686–2698. DOI: 10.1109/tnnls.2016.2598655. URL: <https://doi.org/10.1109/tnnls.2016.2598655>.
- [3] A. Bernal, S. Fok, and R. Pidaparthi. “Financial Market Time Series Prediction with Recurrent Neural Networks”. In: (2012). URL: <http://citeseerx.ist.psu.edu/viewdoc/download?doi=10.1.1.278.3606&rep=rep1&type=pdf>.
- [4] Christopher Bishop. *Pattern recognition and machine learning*. New York: Springer, 2006. ISBN: 978-0387-31073-2.
- [5] Eric Black. “Notes on pound-drever-hall technique”. In: *LIGO Technical notes* (1998).
- [6] Volkmar Brückner. “To the use of Sellmeier formula”. In: (May 2014).
- [7] Daniel Brunner and Ingo Fischer. “Reconfigurable semiconductor laser networks based on diffractive coupling”. In: *Optics Letters* 40.16 (Aug. 2015), p. 3854. DOI: 10.1364/ol.40.003854. URL: <https://doi.org/10.1364/ol.40.003854>.
- [8] *C-Band Booster Optical Amplifier BOA 1004P PM Fiber*. Thorlabs. Apr. 2019. URL: <https://www.thorlabs.com/drawings/fd6c1557aa47f7d3-CEC70D3E-9A30-0668-D7B015F14871FFBB/BOA1004P-SpecSheet.pdf>.
- [9] *CEFA-C-BO-HP Series*. v2.5. Keopsys. URL: <http://www.sun-ins.com/lineup3/keopsys/pdf/CEFA-C-BO-HP.pdf>.
- [10] Antoine Dejonckheere et al. “All-optical reservoir computer based on saturation of absorption”. In: *Optics Express* 22.9 (Apr. 2014), p. 10868. DOI: 10.1364/oe.22.010868. URL: <https://doi.org/10.1364/oe.22.010868>.
- [11] *Digilock 110 Feedback Controler Manual*. v05. Toptica. May 2013. URL: https://www.toptica.com/fileadmin/Editors_English/03_products/03_tunable_diode_lasers/04_control_electronics/02_laser_locking_electronics/DigiLock_110/toptica_Digilock_Manual.pdf.
- [12] RWP Drever et al. “Laser phase and frequency stabilization using an optical resonator”. In: *Applied Physics B* 31.2 (1983), pp. 97–105.
- [13] François Duport et al. “Fully analogue photonic reservoir computer”. In: *Scientific Reports* 6.1 (Mar. 2016). DOI: 10.1038/srep22381. URL: <https://doi.org/10.1038/srep22381>.
- [14] Chrisantha Fernando and Sampsa Sojakka. “Pattern Recognition in a Bucket”. In: *Advances in Artificial Life*. Springer Berlin Heidelberg, 2003, pp. 588–597. DOI: 10.1007/978-3-540-39432-7_63. URL: https://doi.org/10.1007/978-3-540-39432-7_63.

- [15] Gene Franklin. *Feedback control of dynamic systems*. Boston: Pearson, 2015. ISBN: 9780133496598.
- [16] Alireza Goudarzi et al. “A Comparative Study of Reservoir Computing for Temporal Signal Processing”. In: *CoRR* abs/1401.2224 (2014).
- [17] H. Jaeger. “Harnessing Nonlinearity: Predicting Chaotic Systems and Saving Energy in Wireless Communication”. In: *Science* 304.5667 (Apr. 2004), pp. 78–80. DOI: 10.1126/science.1091277. URL: <https://doi.org/10.1126/science.1091277>.
- [18] H. Jaeger. *The "echo state" approach to analysing and training recurrent neural networks*. 2001.
- [19] Herbert Jaeger. “Adaptive Nonlinear System Identification with Echo State Networks”. In: *Proceedings of the 15th International Conference on Neural Information Processing Systems*. NIPS’02. Cambridge, MA, USA: MIT Press, 2002, pp. 609–616. URL: <http://dl.acm.org/citation.cfm?id=2968618.2968694>.
- [20] Herbert Jaeger. “Tutorial on training recurrent neural networks, covering BPPT, RTRL, EKF and the echo state network approach”. In: *GMD-Forschungszentrum Informationstechnik, 2002*. 5 (Jan. 2002).
- [21] Herbert Jaeger et al. “Optimization and applications of echo state networks with leaky- integrator neurons”. In: *Neural Networks* 20.3 (Apr. 2007), pp. 335–352. DOI: 10.1016/j.neunet.2007.04.016. URL: <https://doi.org/10.1016/j.neunet.2007.04.016>.
- [22] *Koheras Adjustik E15*. NKT Photonics. URL: <https://www.nktphotonics.com/wp-content/uploads/sites/3/2015/04/koheras-adjustik-e15.pdf?1552493817>.
- [23] M. Lukoševičius and H. Jaeger. “Reservoir computing approaches to recurrent neural network training”. In: *Computer Science Review* 3.3 (Aug. 2009), pp. 127–149. DOI: 10.1016/j.cosrev.2009.03.005. URL: <https://doi.org/10.1016/j.cosrev.2009.03.005>.
- [24] M. Lukoševičius, M. Jaeger, and B. Schrauwen. “Reservoir Computing Trends”. In: *KI - Künstliche Intelligenz* 26.4 (May 2012), pp. 365–371. DOI: 10.1007/s13218-012-0204-5. URL: <https://doi.org/10.1007/s13218-012-0204-5>.
- [25] IH Malitson. “Interspecimen comparison of the refractive index of fused silica”. In: *Josa* 55.10 (1965), pp. 1205–1209.
- [26] Marvin Minsky. *Perceptrons; an introduction to computational geometry*. Cambridge, Mass: MIT Press, 1969. ISBN: 9780262130431.
- [27] *MPX and MPZ Series Low frequencies to 40 GHz Phase Modulators*. iXblue Photonics. URL: <https://photonics.ixblue.com/sites/default/files/2018-12/C-Band%20Phase%20Modulators.pdf>.
- [28] *MX-LN series, 1550 nm band Intensity Modulators*. iXblue Photonics. URL: <https://photonics.ixblue.com/sites/default/files/2018-12/NRZ%20DPSK%20RZ%20Intensity%20Modulators.pdf>.
- [29] M Nickerson. “A review of pound drever hall laser frequency locking”. In: *JILA, University of Colorado and Nist* ().
- [30] Y. Paquot et al. “Optoelectronic Reservoir Computing”. In: *Scientific Reports* 2.1 (Feb. 2012). DOI: 10.1038/srep00287. URL: <https://doi.org/10.1038/srep00287>.

- [31] A. Perot and Charles Fabry. “On the Application of Interference Phenomena to the Solution of Various Problems of Spectroscopy and Metrology”. In: *The Astrophysical Journal* 9 (Feb. 1899), p. 87. DOI: 10.1086/140557. URL: <https://doi.org/10.1086/140557>.
- [32] *PMFA Series Polarization Maintaining Optical Fiber Amplifiers*. Pritel. URL: https://www.pritel.com/pdfs/PMFA_R10A.pdf.
- [33] *PXI-5124*. National Instruments. Mar. 2019. URL: <http://www.ni.com/pdf/manuals/3711351.pdf>.
- [34] *PXI-5422*. National Instruments. Nov. 2018. URL: <http://www.ni.com/pdf/manuals/371400f.pdf>.
- [35] F. Rosenblatt. “The Perceptron: A Probabilistic Model for Information Storage and Organization in The Brain”. In: *Psychological Review* (1958), pp. 65–386.
- [36] Stuart Russell. *Artificial intelligence : a modern approach*. Upper Saddle River, New Jersey: Prentice Hall, 2010. ISBN: 978-0-13-604259-4.
- [37] Guy Van der Sande, Daniel Brunner, and Miguel C. Soriano. “Advances in photonic reservoir computing”. In: *Nanophotonics* 6.3 (Jan. 2017). DOI: 10.1515/nanoph-2016-0132. URL: <https://doi.org/10.1515/nanoph-2016-0132>.
- [38] Benjamin Schrauwen, David Verstraeten, and Jan Campenhout. “An overview of reservoir computing: Theory, applications and implementations”. In: Jan. 2007, pp. 471–482.
- [39] *TIA-525 Optical/Electrical Converter*. Terahertz Technologies Inc. Apr. 2011. URL: <http://www.terahertztechnologies.com/pdfmanuals/TIA525-Manual.pdf>.
- [40] Fabian Triefenbach et al. “Phoneme Recognition with Large Hierarchical Reservoirs”. In: *Advances in Neural Information Processing Systems 23*. Ed. by J. D. Lafferty et al. Curran Associates, Inc., 2010, pp. 2307–2315. URL: <http://papers.nips.cc/paper/4056-phoneme-recognition-with-large-hierarchical-reservoirs.pdf>.
- [41] Kristof Vandoorne et al. “Experimental demonstration of reservoir computing on a silicon photonics chip”. In: *Nature Communications* 5.1 (Mar. 2014). DOI: 10.1038/ncomms4541. URL: <https://doi.org/10.1038/ncomms4541>.
- [42] Kristof Vandoorne et al. “Toward optical signal processing using Photonic Reservoir Computing”. In: *Optics Express* 16.15 (July 2008), p. 11182. DOI: 10.1364/oe.16.011182. URL: <https://doi.org/10.1364/oe.16.011182>.
- [43] D. Verstraeten, B. Schrauwen, and D. Stroobandt. “Reservoir-based techniques for speech recognition”. In: *The 2006 IEEE International Joint Conference on Neural Network Proceedings*. IEEE, 2006. DOI: 10.1109/ijcnn.2006.246804. URL: <https://doi.org/10.1109/ijcnn.2006.246804>.
- [44] Quentin Vinckier et al. “High-performance photonic reservoir computer based on a coherently driven passive cavity”. In: *Optica* 2.5 (Apr. 2015), p. 438. DOI: 10.1364/optica.2.000438. URL: <https://doi.org/10.1364/optica.2.000438>.
- [45] *WaveShaper 4000S Multiport Optical Processor*. Finisar. Nov. 2014. URL: https://www.finisar.com/sites/default/files/downloads/waveshaper_4000s_product_brief_11_14.pdf.